Investigations of Mixed-Anion Analogs of Manganite Perovskites and Bimetallic Group II Nitride Fluorides

By

Oscar Kipruto Keino

Submitted in Partial Fulfillment of the Requirements

For the Degree of

Master of Science

in the

Chemistry

Program

YOUNGSTOWN STATE UNIVERSITY

December, 2017

Investigations of Mixed-Anion Analogs of Manganite Perovskites and Bimetallic Group II Nitride Fluorides

By

Oscar Kipruto Keino

I hereby release this thesis to the public. I understand that this thesis will be made available from the Ohio LINK ETD Center and the Maag Library Circulation Desk for public access. I also authorize the University or other individuals to make copies of this thesis as needed for scholarly research.

Signature:

_____
Oscar Kipruto Keino, Student   Date

Approvals:

_____
Dr. Timothy R. Wagner, Thesis Advisor   Date

_____
Dr. Sherri Lovelace-Cameron, Committee Member   Date

_____
Dr. Allen Hunter, Committee Member   Date

_____
Dr. Salvatore A. Sanders,   Date
Dean, College of Graduate Studies

ABSTRACT

Lanthanum manganites are perovskite related materials known in particular for their colossal magnetoresistance (CM) properties. Manganite compositions showing CM behavior are mixed cation compounds such as $(Ca_xLa_{1-x})MnO_3$, which contain Mn ions in mixed Mn^{3+} and Mn^{4+} oxidation states.

The goal of this project was to prepare mixed anion analogs of the $LaMnO_3$ oxide phase such that mixed Mn^{3+}/Mn^{4+} oxidation states are introduced by anion rather than cation substitutions. Particular compositions targeted were $La_2Mn_2O_6F$, $Ca_2Mn_2O_5F$ and $Ca_2Mn_2O_4N$. A single step low temperature fluorine insertion process was proposed for synthesis of $La_2Mn_2O_6F$ using various fluorine insertion agents, namely: PVDF, CuF_2, and XeF_2; while standard ceramic methods were proposed for synthesis of the latter two compounds. All of these syntheses techniques were unsuccessful, with the possible exception of the fluorine insertion reaction using PVDF. These results will be summarized, and suggestions for future work will be given.

A second area of focus involved synthesis and characterization of compounds in the Sr-M-N-F system, where M = Mg or Ca. Very few bimetallic N-F compounds have been previously reported. In this work, a new phase of ideal composition SrCaNF was prepared with a doubled cubic (relative to M_2NF rocksalt-type) structure. This phase is highly disordered, and its crystal chemistry will be presented. A Sr_2NF rock salt-type phase was also prepared and analyzed in this study, and to our knowledge is the first single crystal X-ray analysis performed for Sr_2NF, previously studied only through powder X-ray diffraction methods.

ACKNOWLEDGEMENTS

TABLE OF CONTENTS

CHAPTERS

LIST OF FIGURES

FIGURE

LIST OF TABLES

TABLE

LIST OF REACTIONS

CHAPTER ONE

INTRODUCTION

1.1 Introduction to Solid State Chemistry

Solid State Chemistry and Materials Science play a major role in the field of chemistry through the study of crystal structure defects and how to control them in order to obtain improved, desirable electrical and magnetic properties. Solid state materials' characterization plays a central role in determining the relationship between the structure, the properties, and the performance in order to design materials that fit the performance criteria for specific applications. This is conveniently represented in the form of a tetrahedron, generally known as the material science paradigm as shown in **Figure 1.1** below.
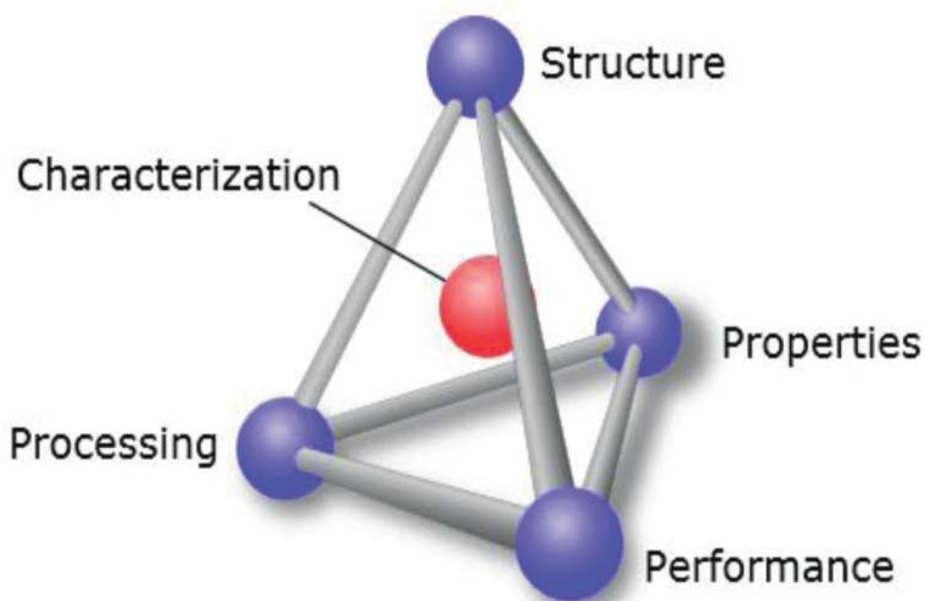
Fig. 1.1 The Materials Tetrahedron (Retrieved July 24, 2017, from https://commons.wikimedia.org/wiki/File:Materials_science_tetrahedron;structure,_proce ssing,_performance,_and_proprerties(sic).svg)

The materials tetrahedron clearly implies that structure is connected to the materials properties, processing, and performance. Materials that have different structures show promise for different applications. Carbon is an excellent example due to very different properties exhibited by its allotropes such as Graphite and Diamond.

Graphite is used in lubricants because of its giant covalent macromolecular structure with 2-D layers connected to each other by weak Van der Waals interactions. The graphite structure is shown in **Figure 1.2.** The layers are bonded in hexagonal rings of carbon atoms. Within each layer, intramolecular covalent bonds attach each carbon atom to three other carbon atoms. The carbon rings have a delocalized bonding whereby the electrons are mobile within the layers. These electrons set up temporary dipole interactions responsible for the Van der Waal's intermolecular forces that hold the layers together. Graphite acts as a lubricant since the weak Van der Waal's forces between the layers allow them to slide over each another. That is the also the reason graphite is used in pencils for writing, i.e. the layers of carbon atoms are rubbed off and stick to the paper. Finally, its structure makes it insoluble in water, as the intramolecular covalent bonds between the carbon atoms are too strong to interact with water. (Clark, 2012).
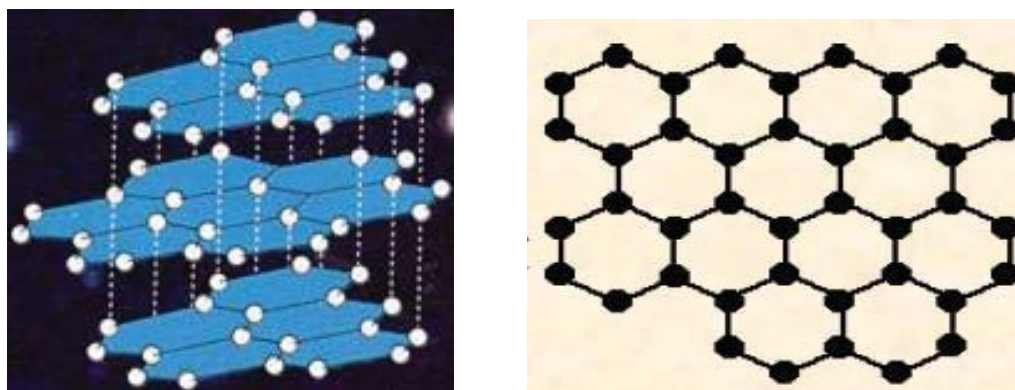
Fig. 1.2 Structure of Graphite (www.chemguide.co.uk/atoms/structures/giantcov)

Though diamond and graphite are both allotropes of carbon, graphite has low density compared to diamond. This is because of the relatively large amount of space between the layers. Whereas graphite is a naturally very soft substance, diamond is the hardest natural substance known because of its different cubic crystalline structure, shown in **Figure 1.3**. All four outer valence electrons in each carbon atom are involved in forming strong covalent bonds with four other carbon atoms, making diamond a strong rigid structure. This hardness plays a critical role in diamond's use as the hardest cutting tool known to exist. Parts of cars, planes, and other machines are shaped by diamond saws. Also, since the valence electrons are not free to move, diamond is a non-conductor of electricity (Clark, 2012).
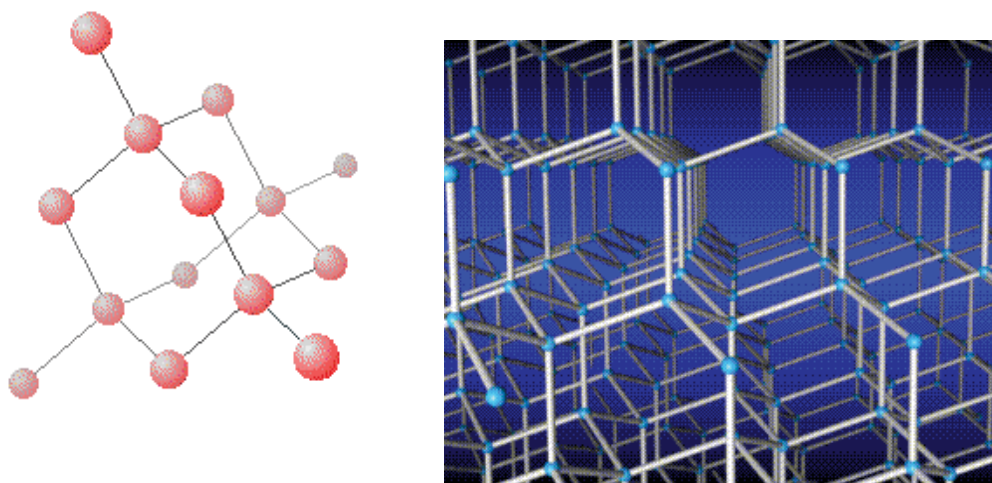
Fig 1.3 Structure of Diamond. (chemguide.co.uk/atoms/structures/giantcov.html)

Properties and performance may have the same use in material science, when the properties of a compound are well defined it becomes easy to learn how it will be used in different applications. Performance is an element of material science that takes into consideration all the work put into the synthesis of a desired material. There is a greater

interest when there is an improved performance in the materials and this gives room for more improvement in the research, because understanding the history of how a material was processed leads to better understanding of its properties and performance.

Synthesis and processing is a significant step in materials chemistry; it's more of an engineering aspect and involves the design of a material with the preferred micro/nanostructure. From an engineering standpoint, a material cannot be used in industry if no economical manufacturing method for it has been developed. Thus, the processing of materials is very important to successful applications emerging from materials science research.

1.2 Solid State Synthesis

Solid state materials synthesis involves a number of applications such as temperature manipulation, mixing of the starting materials, heating and cooling rate as this significantly influences the end product, most ceramic materials require a clear stoichiometric method.

Most of the experiments conducted in solid state reactions are run at high temperature and perhaps under high purity nitrogen or other gas environments. Experiments that are conducted in such a manner require specialized programmable furnaces such as the one shown in **Figure 1.4**, which was the main furnace used in this research. Both sides of the furnace are fitted with tubes to permit dynamic flow of gas, such as nitrogen or argon that aids in creating an inert environment. Care should be taken though, because the tubes fitted in it should be able to withstand high temperature and the choice of the reacting starting material.

Fig 1.4 High temperature (Thermolyne 59300) programmable Oxygen free tube furnace for nitrogen gas experiment.

Solid state reactions involve experimental procedures which use different temperature and reaction atmosphere conditions. **Figure 1.5** below shows one of the smaller programmable furnaces used in this thesis a Mellen furnace with maximum temperature of 1200°C. The furnace is small enough to be operated inside of a fume hood, and was used mainly for ammonolysis reactions. One end of the tube is fitting with a glove bag to provide the inert argon atmosphere needed to manipulate any air sensitive materials to be inserted into the furnace.

Fig 1.5 The programmable tube furnace (Mellen, NACCI series) utilized primarily for ammonolysis reactions in our lab.

 A In order to prepare a powder mixture for reaction in the solid state, a hydraulic press is often used to agglomerate the starting material to a pellet form. This technique aids ceramic materials to undergo uniform reaction conditions and to react more effectively by placing reactants in closer contact. Pellets formed are mainly in the shape of a tablet.
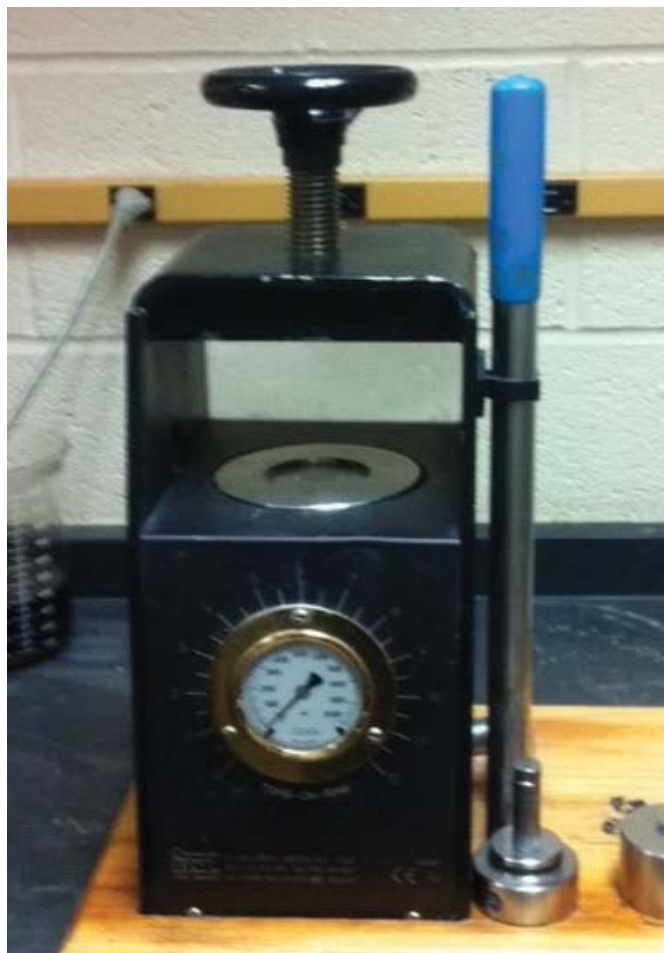
Fig 1.6 A hydraulic press used to compress starting materials for solid state, high temperature synthesis into pellets for more effective reactions.

Prior to forming a pellet using a hydraulic press, a mixer mill as shown in **Figure 1.7** is often used to mix and pulverize ceramic starting materials to analytical fineness. The vial inserted into the mill contains a sample with two hard ceramic balls to pulverize the sample, and should be 2/3 filled with the materials to be mixed to prevent the two small balls from grinding against each other. The end product will often yield a finely divided and well-mixed powder.

Fig 1.7 SPEX mixer mill available in this work for preparation of powder reaction mixtures.

1.3 X-ray Powder Diffraction (XRPD)

X-ray powder diffraction (XRD) is one of the main analytical techniques used in this thesis, specifically for purity verification of starting materials and phase identification of product mixtures of our reactions. The instrument that was readily available at YSU for X-ray powder diffraction is the Rigaku Miniflex II (shown in **Figure 1.8**), which is equipped with a Cu X-ray tube and an automated sample changer that can be used to run six different samples in standard operation.

Fig 1.8 YSU Rigaku Miniflex II, which was used for X-ray Powder diffraction used in this work.

The technology behind X-ray diffraction is based on constructive interference of monochromatic X-rays interacting with a crystalline sample. These X-rays are generated by a cathode ray tube, filtered to produce monochromatic radiation, collimated to concentrate, and directed toward the sample. X-ray diffractometers consist of three basic elements: an X-ray tube, a sample holder, and an X-ray detector.

X-rays are on the electromagnetic spectrum between gamma rays and ultraviolet rays and the X-rays used in diffraction experiments are produced when a beam of electrons accelerated from a tungsten filament collides with a metal target. Normally the

metal is either Cu, Fe, Mo, or Cr, although usually copper is used. After being accelerated through 30-50 kV, high-energy electrons ionize some of the 1s electrons of copper, after which a 2p or 3p electron immediately drops down to occupy the 1s level, resulting in emission of X-ray radiation as energy is released. When the electrons in copper transition from 2p levels the X-ray radiation is referred as K_α, with a wavelength of 1.5418Å. When electrons transition from 3p it is referred as K_β, with wave length of 1.3922 Å.

There is further subdivision of wavelengths arising from the 2p $\rightarrow$ 1s transition, depending on initial spin state of the 2 p electron, and these are referred to as $K_{\alpha1}$ and $K_{\alpha2}$ X-rays with wavelengths of 1.54051Å and 1.5433 Å, respectively. These are averaged when referring to K_α radiation in general. Of the Kα and K_β X-rays, $K_{\alpha1}$ are the most intense and are normally used to characterize the target material compound. Most modern diffractometers are equipped with a monochromator to filter out $K_{\alpha2}$ radiation before the beam reaches the sample.

Max von Laue discovered in 1912 that crystalline substances act as three-dimensional diffraction gratings for X-ray wavelengths, which are similar to the spacing of planes in a crystal lattice. William Lawrence Bragg later introduced an equation now known as Bragg's Law, which relates the angle of incidence of an X-ray beam on a set of crystal planes to the interplanar spacing such that diffraction intensity is observed.

Figure 1.9 shows a set of planes (hkl) a distance d apart, with X-rays reflecting from each plane. When the additional path length (= 2dsinθ) of subsequent waves is an integral number of wavelengths, constructive interference occurs, and diffraction intensity is observed.   When the incident angle is anything but the Bragg angle, the

reflected rays interfere destructively because they are out of phase.

Fig 1.9 Bragg's Law (http://skuld.bmsc.washington.edu/merritt/bc530/bragg)
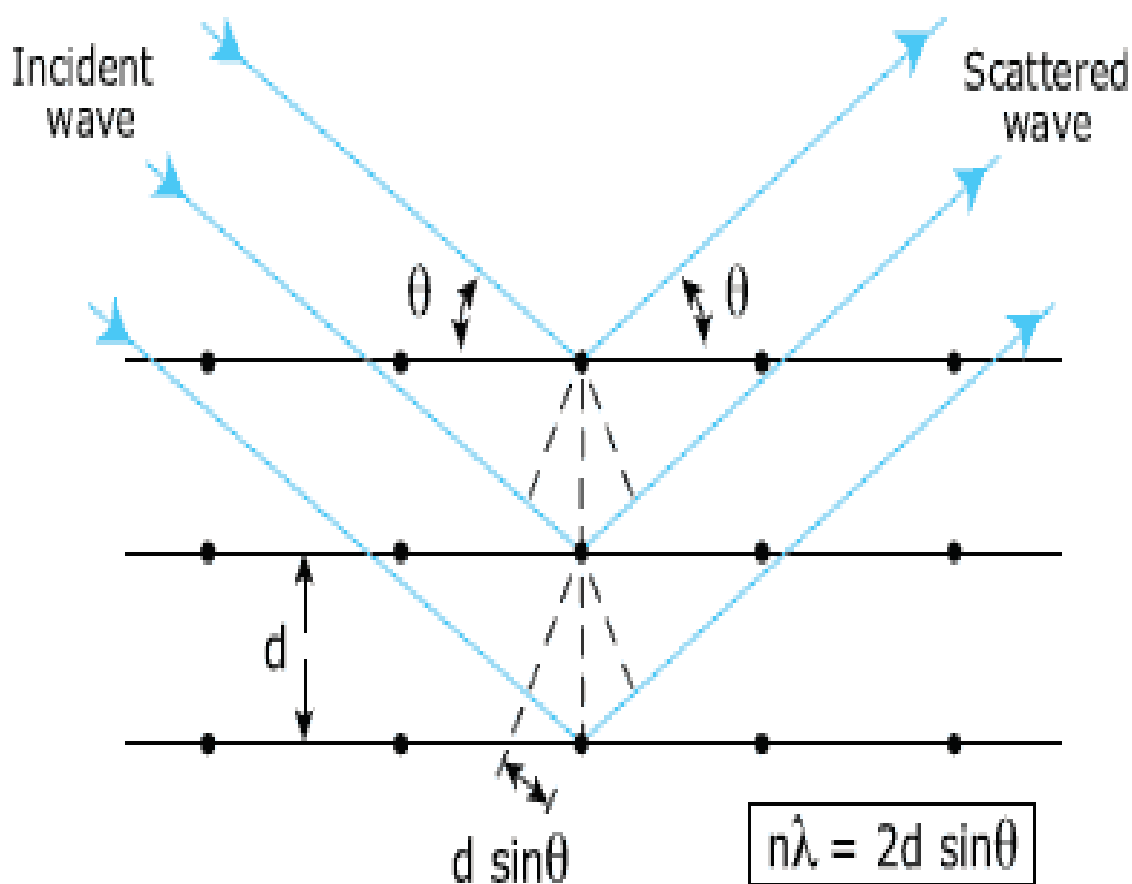
Bragg's Law is exhibited by the mathematical formula: $n\lambda=2d\sin\theta$ where d is the spacing between layers of atoms at the vertical distance between two parallel planes, θ is the angle between the incident rays and the surface of the crystal and is commonly referred as the Bragg's angle, and λ is the wavelength of the X-rays. The quantity n is the order of reflection, and is always a whole number ≥ 1. When $n = 2$, for example, then a reflection can only be achieved when the Bragg angle θ is big enough such that Bragg's Law still holds for the set of planes diffracting. This case is referred to as a second order

reflection. Note that although the d spacing for this reflection would appear to be one-half the value of the first order reflection, there is not necessarily a set of planes with spacing ½ d physically present.

1.4 X-ray Crystallography

Single crystal X-ray diffraction analysis is best known for use in quantitative structure determination of unknown single crystalline materials. X-ray crystallography was widely used as a standard measurement technique in solving crystal structures in this thesis, and the required instrumentation is readily available at YSU.

Though three different single crystal diffractometers are available in the YSU X-ray diffraction facility, the use of the Bruker D8 QUEST was most useful in this research. The YSU Bruker D8 QUEST diffractometer, shown in **Figure 1.10**, is a high resolution instrument equipped with a very high brightness Molybdenum IμS Incoatec micro source; 100 cm^2 Photon 100 Complementary Metal Oxide Sensor detector; Helios optics; kappa 4-axis goiniostat, and variable temperature capabilities (Oxford cryostream 700 plus, 80-500 K). Its core feature is the new CMOS technology, this facilitates the detector data collection speed, as the shutter remains continuously open throughout the data collection. The diffractometer is also equipped with a low temperature system, which was useful for protecting our air sensitive crystals from decomposition during data collection.
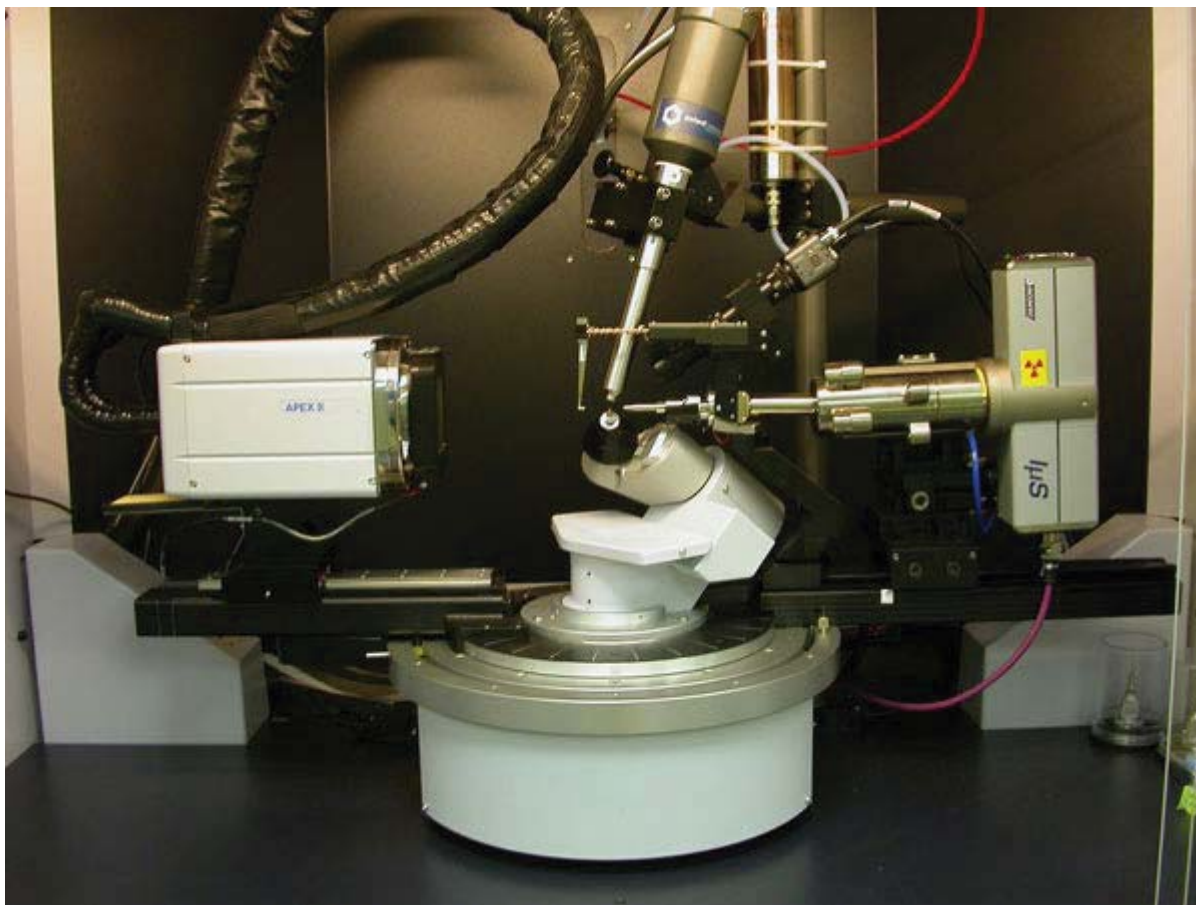
Figure 1.10 YSU single-crystal X-ray diffraction, Bruker Quest instrument used in this research.

1.5 Crystal Systems

There are a total of seven solid state crystalline lattices, and they include the following: Triclinic, Monoclinic, Orthorhombic, Tetragonal, Trigonal, Hexagonal, and Cubic. The seven systems have various structures that are different from one another, and structures of all crystals that exist can be classified according to the symmetry of these systems. In order to define a three dimensional shape of the crystal morphology,

every system is described in terms of unit cell parameters with different edges and angles, consisting of lattice edges a, b, and c and angles α, β and γ **(www.chem.wisc.edu)**

Table 1.1 summarizes the unit cell dimensions of the seven crystal systems. It also shows that the number of lattices associated with each crystal type.

Table 1.1 The seven crystal systems.

Crystal Lattice	Cell Dimensions	Interfacial Angles	Number of Lattices
Cubic	$a = b = c$	$\alpha = \beta = \gamma = 90^0$	3
Tetragonal	$a = b \neq c$	$\alpha = \beta = \gamma = 90^0$	2
Orthorhombic	$a \neq b \neq c$	$\alpha = \beta = \gamma = 90^0$	4
Monoclinic	$a \neq b \neq c$	$\alpha = \gamma = 90, \beta \neq 90^0$	2
Hexagonal	$a = b \neq c$	$\alpha = \beta = 90, \gamma = 120^0$	1
Rhombohedral	$a = b = c$	$\alpha = \beta = \gamma \neq 90^0$	1
Triclinic	$a \neq b \neq c$	$\alpha \neq \beta \neq \gamma \neq 90^0$	1

The lattice points in a unit cell can be arranged as simple, body-centered, face-centered and base centered, and together with the above named seven crystal lattices gives a total of fourteen Bravais lattices, as shown in **Figure 1.11.**
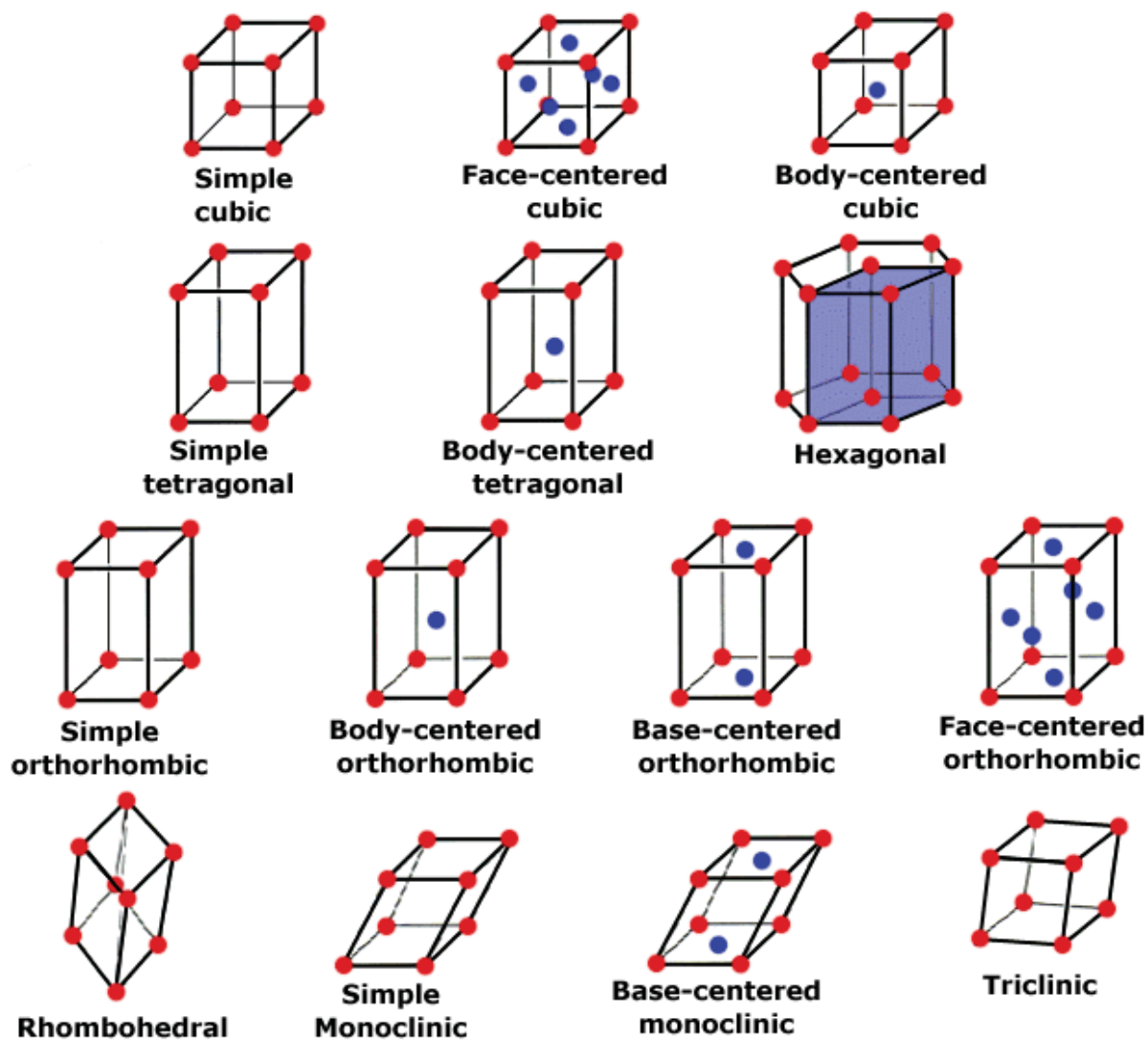
Fig 1.11 Fourteen Bravais lattices (www.seas.upenn.edu/~chem101/sschem/bravais.gif)

CHAPTER TWO

BACKGROUND

2.1 Introduction to Perovskites.

Perovskites are compounds that occur naturally as calcium titanium oxide, $CaTiO_3$, and there are many related perovskite-type compositions and structures that have been reported in the literature. A portion of this thesis is devoted to the study of some manganite perovskites. The ideal composition of a perovskite type material is ABX_3, where A& B are cations while X is an anion. If X is an anion with an oxidation state of −2 then cations A and B must have oxidation states that add up to +6, or if X is an anion with an oxidation state of −1, then cations A and B must have an oxidation states adding up to +3. Ideal perovskite-type compounds have a cubic unit cell where the larger A cation is at the cube center, with B cations on the corners and anions at edge centers.
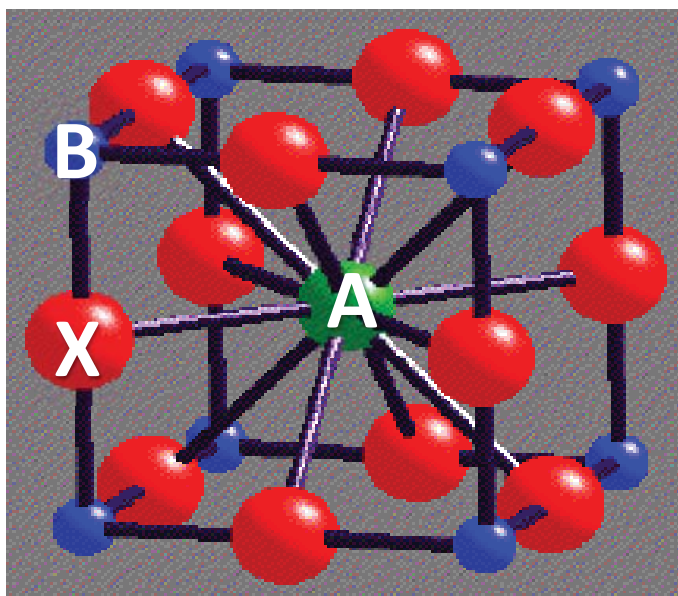
Fig 2.1 An ideal Perovskite-type compound with primitive cubic lattice and composition ABX_3. (www.ossila.com/pages/perovskites-and-perovskite-solar-cells)

Figure 2.1 is an example of an ideal perovskite structure of one unit cell. For any cubic unit cell in general the diagonal of the cell is 1.414 times the cell edge, and so an ideal perovskite-type lattice could be represented through the general formula $(R_X + R_A)$ = 1.414($R_X + R_B$), where R_x, R_A, and R_B represent the radii of X, A, and B atoms, respectively. This formula assumes that all atoms in the perovskite unit cell in **Fig 2.1** to be just touching.

Many structural variations can be possibly achieved in perovskites because of the many manipulations and distortions possible due to different relative sizes of A & B cations. The existence of perovskite-related structures that are not always ideal gives rise to the so called tolerance factor, *t*, that can be calculated from the relationship mentioned above: $R_X + R_A = t * 1.414(R_X + R_B)$, where t is the tolerance factor and has a value of one in the ideal cubic case. Rearranging, the degree of distortion can be estimated using the equation. (Liu et.al. 2008)

$$t = \frac{\text{radius (A)} + \text{radius(X)}}{\sqrt{2} \, [\text{radius (B)} + \text{radius(X)}]}$$

The cubic structure is usually stable when the tolerance factor is $0.985 < t < 1.06$. Thus $CaTiO_3$ which has a tolerance factor of 0.973, has an orthorhombic rather than cubic structure.

2.2 Manganite Perovskites

$LaMnO_3$ is antiferromagnetic and acts as an insulator but these properties can be manipulated by cation substitution, such as partial substitution of La^{3+} by Sr^{2+} or Ca^{2+}, as in the formula $Ca_{0.4}La_{0.6}MnO_3$. This substitution results in oxidation of some Mn^{3+} to

Mn^{4+}, which is an important factor in magnetic properties discussed in the next section.

Table 2.1 lists the structural properties and tolerance factors (calculated as per Section

4.2) of $AMnO_3$ compounds, where A= Ca, La and a mixed Ca-La phase.

Table 2.1 Tolerance factors of some known compounds.

Manganite Compound	Structure	Magnetic Property	Tolerance Factor
$CaMn^{4+}O_3$	Monoclinic	Non-magnetic	1.011
$LaMn^{3+}O_3$	Rhombohedral	Non-magnetic (Oxidative non-Stoichiometry)	0.960
$Ca_{0.4}La_{0.6}(Mn^{3+})_{0.6}(Mn^{4+})_{0.4}O_3$	Orthorhombic	Colossal Magnetoresistive	0.979

2.3 Colossal Magnetoresistance.

Colossal magnetoresistance (CMR) refers to the change in electrical resistivity of

materials by several orders of magnitude upon exposure to a magnetic field. Change in

resistance of conventional materials displaying magnetoresistance is approximately 5%.

(Liu *et al*., 2013). It was discovered that when $LaMnO_3$ is partly substituted with Sr, a

CMR material results. The CMR effect shown in $La_{1-x}Sr_xMnO_3$ where x=0.3 in **Figure**

2.2 displays a resistivity decrease by a several orders of magnitude at a certain

temperature upon exposure to a magnetic field. Thus at low temperature the material

behaves as a conductor and acts as an insulator at high temperature.
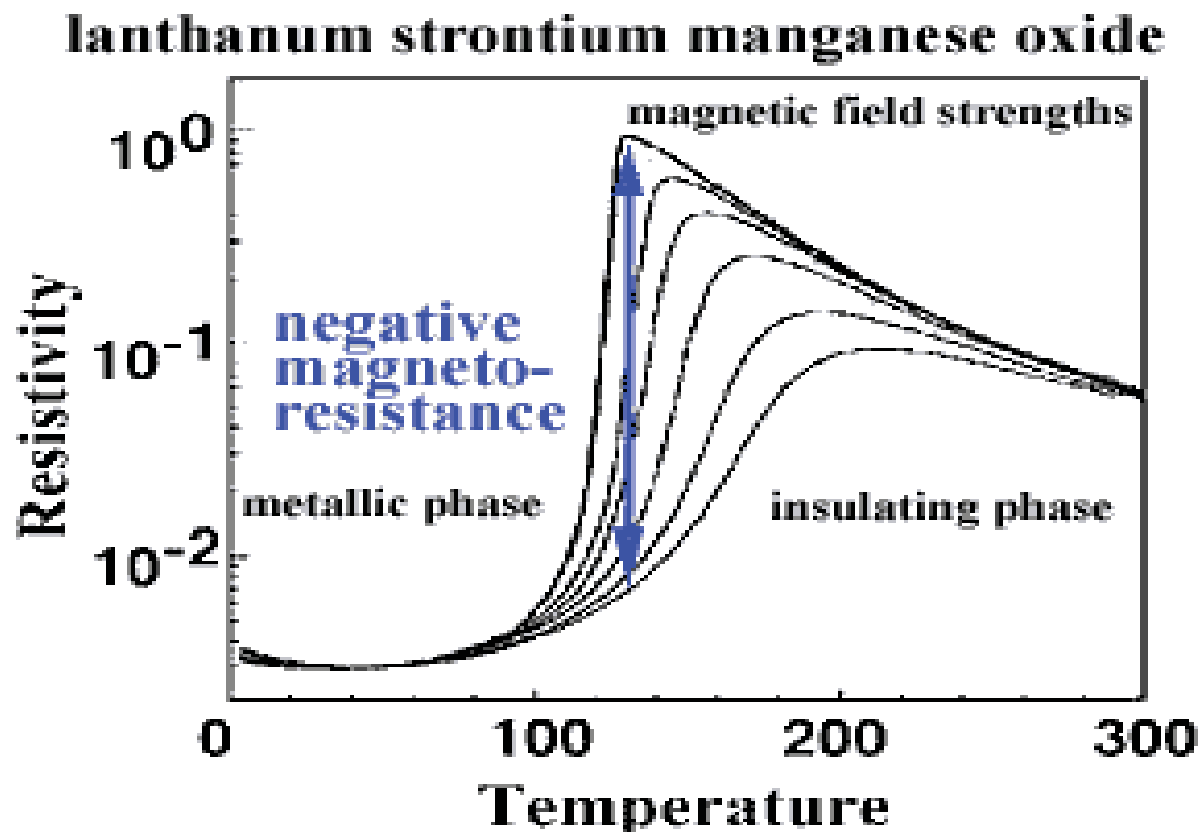
Fig 2.2 CMR behavior for doped (La, Sr)MnO$_3$
(www.lbl.gov/ScienceArticles/Archive/colossal-magnetoresistance.html)

This behavior is thought to be as a result of a strong electron phonon coupling

effect of Jahn-Teller distortion. As mentioned, the compound La$_{1-x}$Sr$_x$MnO$_3$ contains

Mn^{3+} which is a d^4 ion, and Mn^{4+}, a d^3 ion. This mixture of oxidation states gives rise to a

so called double exchange interaction, thought to be related to the CMR effect as

explained by (Baldini *et. al.* 2015).

2.4 Double Exchange Mechanism

According to Pavarini *et. al.* (2012), double exchange is a ferromagnetic exchange interaction between two atoms. Ferromagnetic exchange means electron spins remain aligned throughout the exchange. Double exchange is facilitated when the atoms have different oxidation states such that the itinerant delocalized electron does not have to change spin and conforms with Hund's Rules when moving to the acceptor atom. An optimal example for this explanation is double exchange within Mn^{3+}-O-Mn^{4+} linkages in Ca or Sr-doped La manganite perovskites, as indicated in **Figure 2.3** below.
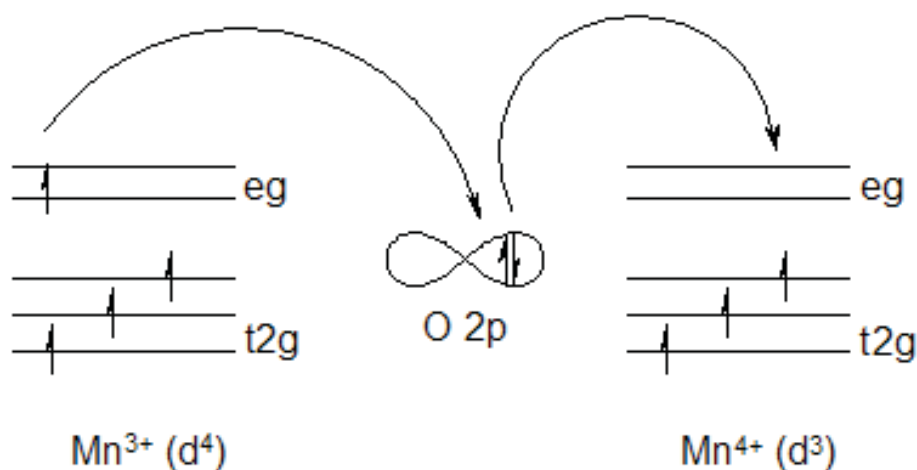
Fig. 2.3 The double exchange mechanism. (Baker, 2010)

The transfer of electron from Mn^{3+} to Mn^{4+} ions is the basic mechanism of electrical conduction in manganites, governed by double exchange interaction involving the simultaneous jump of the e_g electron of Mn^{3+} to the oxygen p-orbital, and the electron with same spin from the oxygen p-orbital jumping to the empty e_g orbital of Mn^{4+} leading to a ferromagnetic state (Zener, 1951). In manganites with strong double exchange interaction, the e_g electrons become delocalized for a certain doping range at low

temperature, this leads to metallic behavior. Because the delocalized electron interaction can be enhanced in a magnetic field by aligning the spins at adjacent Mn-O-Mn ions, the conductivity increases (Hwang *et.al.* 1996).

It is worth noting that the CMR effect is enhanced as the Mn^{3+}-O-Mn^{4+} bond angle approaches 180°, or as the perovskite tolerance factor discussed previously approaches 1.0, because this results in optimal overlap in adjacent e_g orbitals creating a wider e_g band gap. Non-cubic perovskites with tolerance factors smaller or greater than 1.0 usually show tilting of octahedra, such as seen for MnO_6 octahedra in **Figure 2.4** below. While tilting does help to optimize the bond distance in the lattice, it does result in the Mn^{3+}-O-Mn^{4+} bond angle dropping below 180°. As discussed in the Chapter 4, the mixed anion phases targeted in this study was designed in part by optimization of the tolerance factor.
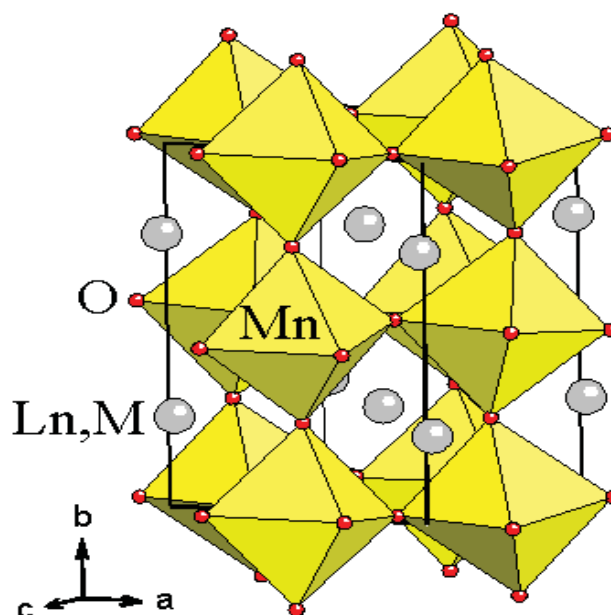
Fig 2.4 Structure for perovskite-like (La, M) MnO_3 phases (www.attfield.ch.cam).

2.5 Alkaline Earth Metal Nitride-Fluorides

The oxides of alkaline earth metals can be effectively substituted where the O^{2-} ions can be replaced by N^{3-} and F^-, leading to alkaline earth nitride fluorides of composition M_2NF (M = Mg, Ca, Sr and Ba). The earliest experiments were conducted by Andersson (1970) and entailed his research primarily on magnesium nitride fluoride. In these studies, three different phases in the Mg-N-F systems were reported which Andersson referred to as "pseudo oxides".

Mg_3NF_3 was one of the phases reported, and was a product of the reaction of Mg_3N_2 and MgF_2 between 900° and 1050°C. The structure is rocksalt-type, but with a vacant Mg^{2+} cation site and N^{3-} and F^- ions sharing the anion position. The space group was reported as $Pm\overline{3}m$, with cell parameter a = 4.216 Å, Z=1. More recently, this phase was verified in a powder neutron diffraction study by Brogan *et al*. (2012).

The second polymorph was a tetragonal phase designated as L-Mg_2NF, with space group $I4_1/amd$ and a = 4.186 Å, c = 10.042 Å. Thus N and F atoms are ordered along the c-axis but not along the a or b axes. Anderson reported this structure as being intermediate between rocksalt and zinc blende. Further high temperature manipulation led to H-Mg_2NF, a third polymorph reported as being isostructural with rocksalt-type MgO. A later neutron powder diffraction study by Brogan *et al*. (2012) confirmed the Mg_3NF_3 and L-Mg_2NF previously reported by Andersson (1970).

Ehrlich *et al*. (1971) extended Andersson's study to include alkaline earth M_2NF compounds for M = Ca, Sr , and Ba. Using X-ray powder diffraction, they found all three nitride-fluorides to be isostructural with the rocksalt-type MO analogs. Galy *et al*. (1971) also reported rocksalt-type Ca_2NF in their X-ray powder diffraction study.

Experiments conducted by Nicklow *et al*. (2001) involved the synthesis and studies for the first time of a single crystal structure of Ca_2NF, whereas previous reports for M_2NF (M = Mg, Ca, Sr, and Ba) compounds were all based on X-ray powder diffraction studies. The preparation by Nicklow *et al*. involved using starting materials of calcium and calcium fluoride and heating under N_2 in a high temperature programmable tube furnace. The Ca_2NF crystals obtained were yellow in color and as expected, were air sensitive. The sample was also isostructural with L-Mg_2NF, and not the disordered rocksalt–type phase reported by Ehlrich *et al*. (1971) and Galy *et al*. (1971). X-ray data collected also revealed that the single crystal structure had a space group of $I4_1/amd$, unit cell parameters a = 4.901 Å and c = 10.516 Å.

The second single crystal study by Wagner (2002) reported an ordered rocksalt-type phase for Sr_2NF, which was the first time this phase was observed for the M_2NF system in general. The synthesis involved the mixture of strontium metal and SrF_2 in a 3:1 stoichiometric ratio, reacted at a temperature of 1000ºC in a constant flow of nitrogen gas. Two isostructural crystals were actually analyzed in the study, one a brownish-yellow (BY) Sr_2NF sample with a = 10.6920(45) Å, and the other a dark red (DR) Sr_2NF crystal with a = 10.7655(20) Å. The structure for both crystals had a unit cell which is doubled compared to the disordered rocksalt-type cell due to ordering of N and F atoms along all three cell axes. Interestingly, the X-ray data sets for both crystals showed extra electron density at an interstitial tetrahedral site in the lattice. This was refined as a Frenkel defect, with F atoms at octahedral lattice positions displaced to the interstitial site.

Jack *et al.* (2005) focused on a study of Ca_2NF crystals grown from the melt of a mixture of Ca metal and CaF_2 in a 3:1 stoichiometric ratio. The reaction yielded Ca_2NF crystals that were yellow in color and air sensitive. Single crystal X-ray structure analysis from the selected sample revealed an ordered rocksalt-type phase with approximately doubled lattice relative to the Ca_2NF rocksalt-type structure, similar to the phase observed in the Sr_2NF system reported by Wagner (2002) discussed above. The lattice parameter for the doubled cubic Ca_2NF phase was determined to be 10.0215(8) Å, with space group $Fd\bar{3}m$ (No. 227). This is slightly more than twice the cell parameter of 4.937 Å reported for disordered rocksalt-type Ca_2NF by Ehrlich *et al.* (1971). **Figure 2.5** shows that the doubled cell is due to ordering of N and F atoms along all three cell axes.
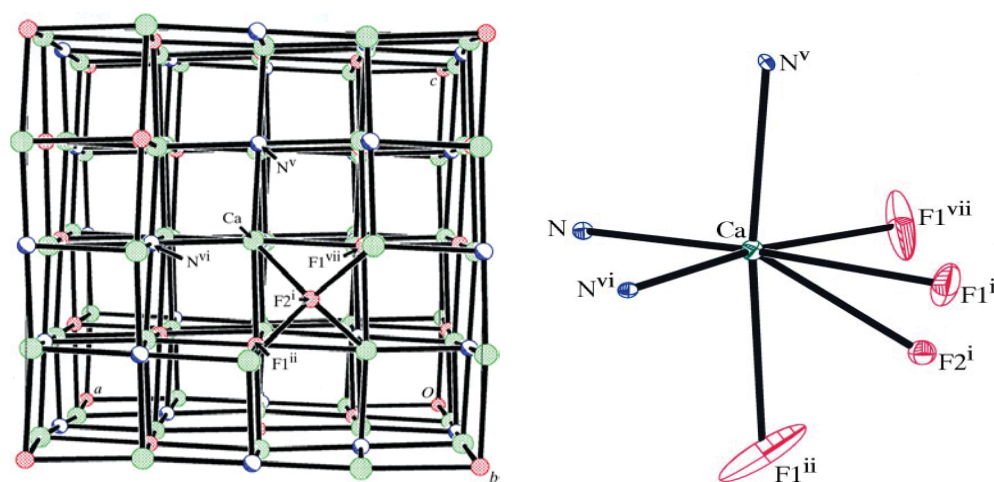
Fig 2.5 Unit cell and a coordination sphere for Ca in Ca_2NF (Jack *et al.*, 2005).

As observed for the Sr_2NF doubled cubic phase discussed above, the doubled cubic Ca_2NF lattice reported by Jack *et al.* (2005) showed disorder at the F octahedral position. This is evident from the large displacement parameters for the F1 octahedral position seen in Figure 2.5. There were also F atoms observed at interstitial tetrahedral

sites, which were refined as Frenkel defects similar to the case for doubled cubic Sr_2NF.
More recently, Al-Azzawi *et al*. (2017) showed that there is actually a non-stoichiometric
defect operating in the lattice, as will be further discussed below.

Siebel and Wagner (2004) reported the preparation and structure determination of
single crystalline Ba_2NF. In this study, a new approach for synthesis of the M_2NF
compound was utilized. Rather than reacting the metal with metal fluoride, KCuF3 was
reacted with Ba metal at 900 °C in a high temperature programmable tube furnace with a
constant flow of nitrogen gas. The Ba_2NF crystal obtained was dark violet in color and
like other alkaline earth metal nitride fluoride single crystals, it was highly air-sensitive.
Characterization by X-ray diffraction showed that the single crystal Ba_2NF sample was
isostructural with rock-salt type BaO, with space group $Fm\bar{3}m$ and cell parameter a =
5.6796(19) Å, Z =2.

Al-Azzawi (2016) reported the synthesis and structure characterization of
doubled cubic Ca_2NF and a quadrupled mixed metal nitride fluoride phase of
composition CaMgNF. The work on his doubled cubic Ca_2NF phase was recently
published (Al-Azzawi *et al.*, 2017). The Ca_2NF single crystals were synthesized by first
preparing the pure, dry $KCuF_3$ precursor, and reacting this with Ca metal according to the
reaction:

$$KCuF_3 + 4Ca + N_2 \rightarrow 2Ca_2NF + KF + Cu$$
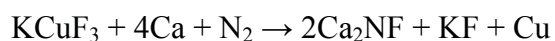
Analysis of one of the resulting yellow Ca_2NF crystals using the chemistry department's new high resolution Bruker QUEST X-ray diffractometer (see Section 1.4) coupled with Energy Dispersive Spectroscopy revealed that the doubled cubic phase is actually nonstoichiometric. The refined composition is $Ca_2N_{0.925}F_{1.23}$, with space group $Fd\overline{3}m$ (No. 227) with a = 10.0301(5) Å and Z = 16. In this structure, F atoms are again positioned at interstitial tetrahedral sites, but instead of charge compensation occurring via a Frenkel defect as considered in the earlier studies discussed above, there is instead partial substitution of F atoms for N atoms on the N octahedral site. Thus, for every two interstitial F atoms, one F atom replaces an N atom in the lattice. **Figure 2.6** shows the F1/F3 shared position and F2 interstitial site.
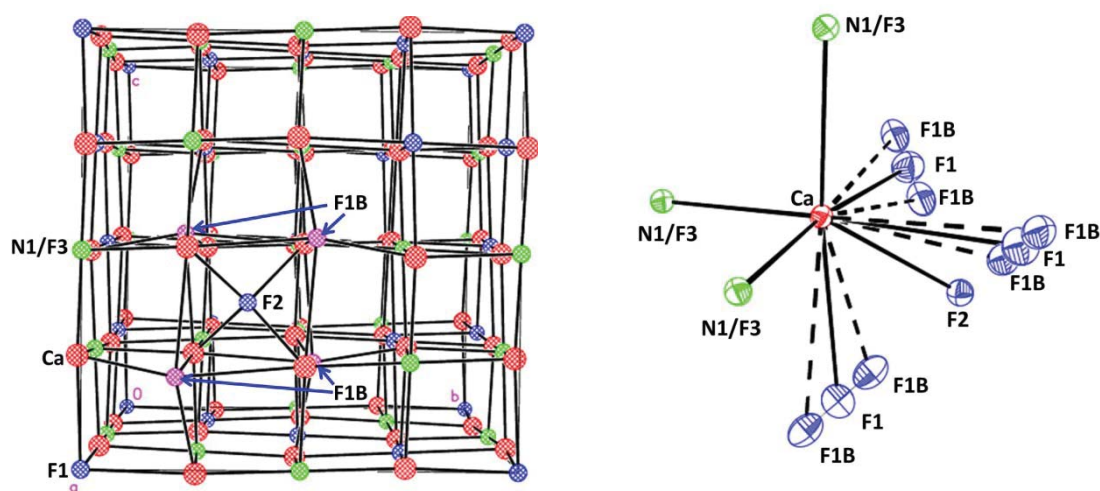
Fig. 2.6 Left: The unit cell for the final Ca_2NF structure by Al-Azzawi *et al*. (2017) showing the ordering of N and F atoms along the cell axes. Also evident is one F2 interstitial position with nearby F1B atoms that were displaced from F1 octahedral sites. **Right**: A view of a Ca coordination sphere in the doubled-cubic Ca_2NF structure, showing disorder at the F1 position.

Also evident in the right part of Figure 2.6 is the highly disordered F1 octahedral position. The F1 sites is actually split into two positions; one at the ideal octahedral site and the other on a position with symmetry equivalent positons 0.575 Å on either side of the octahedral positions. These are labeled as F1B sites in the figure. Refinement of occupancies indicates that for every F2 atom in the lattice (reported by Al-Azzawi *et al*. (2017) as 1.71 atoms per unit cell), there are four F1B positions filled. This suggests that F1 atoms are displaced to an F1B position whenever a nearby F2 site is filled.

Al-Azzawi (2016) further synthesized for the first time a mixed alkaline earth metal nitride fluoride compound, specifically CaMgNF. The reaction employed to prepare the target compound was:

$$MgF_2 + Mg + 2Ca + N_2 \rightarrow 2CaMgNF$$
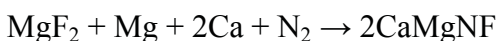
The product mixture contained bright yellow crystals as the final product. X-ray diffraction analysis indicated a cubic unit cell with space group $Fd\overline{3}m$ (No. 227) and cell parameter a = 20.8074(57) Å, which is approximately quadrupled relative to the disordered M_2NF (M = Ca, Sr) rocksalt phase. **Figure 2.7** shows that this is due to ordering of both anions and cations along the cell axes. Unfortunately, the crystal quality was not sufficient to achieve convergence of a final model. However, the data was reliable for unit cell determination.
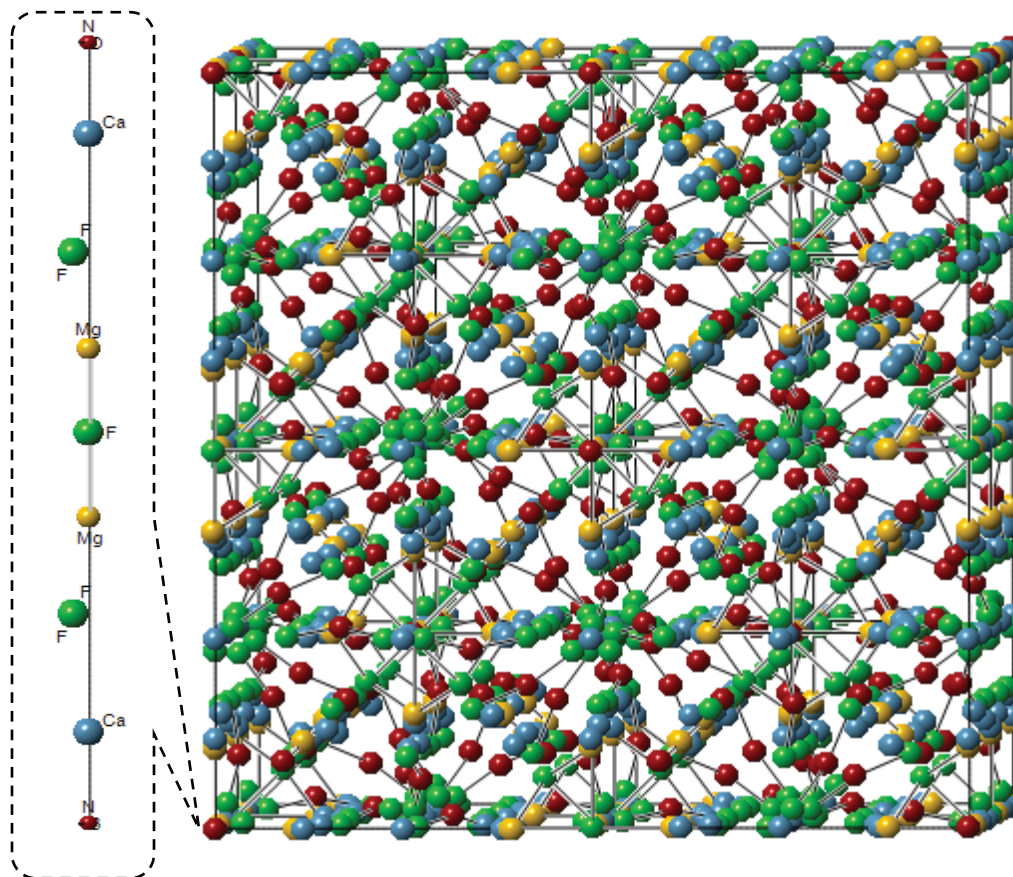
Fig. 2.7 The unit cell for CaMgNF, showing quadrupling of the M_2NF (M= Ca, Sr) disordered rocksalt-type phases or doubling of the ordered rocksalt-type M_2NF phases. Ordering of both cations and anions along the cell axes is evident. (Al-Azzawi, 2016).

To our knowledge, this study by Al-Azzawi (2016) was the first in which a bimetallic alkaline earth metal nitride fluoride compound was successfully prepared. This work has opened further opportunities to explore alkaline earth metal chemistry, and new results in this area will be presented in Chapter 5.

A summary of M_2NF (M = Mg, Ca, Sr, and Ba) phases reported to date is listed in **Table 2.2**.

Table 2.2 Summary of M_2NF (M = Mg, Ca, Sr, and Ba) phases reported to date

Oxide Analog (rocksalt)	Metal Nitride-Fluoride				Bimetallic Nitride-Fluoride
	Tetragonal	**Layered Hexagonal**	**Rocksalt**	**Ordered Rocksalt** **(doubled cubic)**	**Quadrupled Cubic**
MgO	[a, b]L-Mg_2NF		[a]H-Mg_2NF		[j]CaMgNF
CaO	[c]L-Ca_2NF		[e, f]Ca_2NF,	[h]Ca_2NF [k]SrCaNF	
SrO			[e, k]Sr_2NF	[i]Sr_2NF	
BaO		[d]Ba_2NF	[d, e, g]Ba_2NF		

[a]Andersson, (1970); [b]Brogan *et al*., (2012); [c]Nicklow *et al*.; (2001); [d]Bailey *et al*., (2011); [e]Ehrlich *et al*., (1971); [f]Strozewski, (2007); [g]Seibel & Wagner, (2004); [h]Jack *et al*., (2005); [i]Wagner, (2002); [j]Al-Azzawi, (2016); [k]this work.

CHAPTER 3
STATEMENT OF THE PROBLEM

Typically, research in inorganic solid state chemistry has involved property manipulation of oxides through cation substitution. The overall theme of this research is to study the impact on crystal chemistry and properties of certain oxides through anion rather than cation substitution. Two different classes of compounds are studied, the first is related to the CMR (Colossal Magnetoresistive) manganite perovskite materials, and the second is related to Group II (specifically Sr & Ca) rocksalts. In both cases, the compounds targeted for this study have compositions derived from oxides by partial or total replacement of oxide ions by nitride and/or fluoride ions. In the Group II rocksalt system, certain mixed cation nitride fluoride phases are studied for the first time.

Ca-doped $LaMnO_3$ is a well-known CMR material. While a theoretical basis for CMR behavior is not well-established, a key feature of manganite CMR materials is the presence of both Mn^{3+} and Mn^{4+} ions in the lattice. This enables electron mobility through e_g bands in the lattice through a Mn(III)-O-Mn(IV) double exchange mechanism. The goal in this part of the research was to prepare new mixed Mn^{3+}/Mn^{4+} manganites of compositions of $Ca_2Mn^{3+}Mn^{4+}O_4N$, $Ca_2Mn^{3+}Mn^{4+}O_5F$, and $La_2Mn^{3+}Mn^{4+}O_6F$. The first two compositions were targeted by standard ceramic methods and an ammonolysis reaction, respectively. The latter phase was targeted as a fluorine insertion compound, via fluorine insertion of $LaMnO_3$. Three different fluorinating agents were investigated in the syntheses experiments, including CuF_2, XeF_2, and PVDF.

M_2NF compounds, where M is one of the Group II metal ions Mg^{2+}, Ca^{2+}, Sr^{2+}, or Ba^{2+}, have been known for some time. They can be considered as 'derived' from MO rocksalt phases by the replacement of each two O^{2-} ions in the MO lattice by one N^{3-} and one F^- ion. Due to the lower electronegativity of nitrogen relative to oxygen, the band gap in an M_2NF phase tends to be smaller than the corresponding MO phase, affecting optical and electronic properties as well as crystal chemistry. Very few mixed metal nitride fluoride compounds have been studied in general, and no mixed Group II nitride fluoride compounds have been previously reported. In this work, the mixed metal Sr-Ca-N-F system will be studied for the first time. Focus here is on the crystal chemistry of the system.

CHAPTER 4

INVESTIGATION OF MIXED-ANION ANALOGS OF MANGANITE PEROVSKITES

4.1 Introduction

As mentioned in Chapter 2, Ca or Sr-doped perovskite-type $LaMnO_3$ materials are well known for their colossal magnetoresistive (CMR) properties. As also mentioned, while the theoretical basis for CMR behavior is not well established, the presence of mixed Mn^{3+}/Mn^{4+} oxidation states in compositions like $CaMnO_3$ is thought to play an important role in the CMR behavior of these materials. This is due to the mobility of the e_g electron in Mn^{3+} (d^4 config.) through e_g bands of the lattice via a double exchange mechanism (Ramirez, 1997). The purpose of this thesis work was to try to prepare the first mixed-anion analogs of manganite perovskite phases with mixed Mn^{3+}/Mn^{4+} oxidation states, and potential colossal magnetoresistive (CMR) properties. The particular compositions targeted here include: $Ca_2Mn^{3+}Mn^{4+}O_5F$, $Ca_2Mn^{3+}Mn^{4+}O_4N$, and $La_2Mn^{3+}Mn^{4+}O_6F$. Besides the use of mixed anions to enable the presence of Mn^{3+}/Mn^{4+} mixed oxidation states, this choice of compositions was also rationalized in part through analysis of tolerance factors, discussed in the next section.

4.2 Tolerance Factor Analysis of Proposed Compositions

Table 4.1 shows the tolerance factors of the three target phases. As discussed in Chapter 2, tolerance factors give an indication as to whether or not a given perovskite-related composition is likely to be cubic. For general composition ABX_3, the tolerance

factor is calculated using the equation:

$$t = \frac{\text{radius(A)} + \text{radius(X)}}{\sqrt{2}[\text{radius(B)} + \text{radius(X)}]}$$

An ideal cubic perovskite-type structure would have $t = 1$, although in general, cubic

structures exist over the range of 0.985 to 1.06. Compositions outside this range usually

have unit cells with lower symmetry, due to tilted BO_6 octahedra in the structure. Of

relevance here is that as the tolerance factor in perovskite manganite CMR materials

approaches one, the lattice is cubic and the Mn^{3+}–O–Mn^{4+} bond angle approaches 180°.

This means that the overlap of Mn^{3+}/Mn^{4+} e_g bands is stronger, leading to wider e_g bands

and enhanced CMR behavior.

Table 4.1 Tolerance factors of targeted compounds.

Manganite Compounds	Tolerance Factors
$Ca_2Mn^{3+}Mn^{4+}O_4N$ (N-substituted $CaMnO_3$)	0.979
$Ca_2Mn^{3+}Mn^{4+}O_5F$ (F-substituted $CaMnO_3$)	0.983
$La_2Mn^{3+}Mn^{4+}O_6F$ (LaMnO$_3$ F-insertion)	0.989

The tolerance factors in Table 4.1 were calculated using ionic radii taken from

Shannon (1976) that corresponded to the charge and coordination number of the specific

ions for our target compounds. For the ABX_3 perovskite-type composition in general, the

large A cation is 12-coordinated (see Fig. 2.1), B cations are in 6-fold coordination, and

X anions are coordinated by only 2 B cations, since A-O bonds are about 40% longer

than B-O bonds (Moreira and Dias, 2007). The radii values used to calculate tolerance

factors are: Ca^{2+}, 1.34 Å; La^{3+}, 1.36 Å; Mn^{3+}, 0.645 Å; Mn^{4+}, 0.53 Å; F^-, 1.285 Å;

O^{2-}, 1.35 Å; and N^{3-}, 1.46 Å (note that this value is for the 4-coordianted case, as a value

for 2-coordinated N^{3-} was not available). For sites sharing ions (e.g., Mn^{3+}/Mn^{4+}), the

radii of individual ions were averaged. Note that for the anion site in the $LaMn_2O_6F$

insertion compound, F^- would be positioned at an interstitial site and so would not share

the anion site with oxygen. These radii were also used to calculate the tolerance factors

for known compounds shown in Table 2.1, including the known CMR material

$Ca_{0.4}La_{0.6}(Mn^{3+})_{0.6}(Mn^{4+})_{0.4}O_3$, for which t = 0.979. Examination of the tolerance factors

in Table 4.1 shows that all three targeted phases therefore have values favorable for CMR

behavior with t ≥ 0.979, with the F-insertion compound showing the highest value.

4.3 Attempted Synthesis of $Ca_2Mn^{3+}Mn^{4+}O_5F$

Wolf (2011) previously attempted to synthesize $Ca_2Mn_2O_5F$ by using a stepwise

route that first involved preparation of $CaMnO_3$. This compound was successfully formed

following the procedure of Meneghini *et al.* (2005), involving a sol-gel method with

$Ca(NO_3)_2 \cdot 4H_2O$ and $MnCO_3$ as precursors. The next step involved reduction of

$CaMnO_3$ using ammonia gas as outlined by Poeppelmeier *et al.* (1982), with overall

reaction: $CaMnO_3 + 2/3\ NH_3 \rightarrow Ca_2Mn_2O_5 + H_2O + 1/3\ N_2$. The product of this reaction

was next to be fluorinated according to the reaction: $Ca_2Mn_2O_5 + NH_4HF_2 \rightarrow 2CaMnO_2F$

$+ NH_4OH$. The final step proposed to achieve the synthesis of the mixed $Mn^{3+/4+}$ target

compound was: $CaMnO_2F + CaMnO_3 \rightarrow Ca_2Mn_2O_5F$. Unfortunately, only the first step

was successful in the project despite several trials to complete the proposed subsequent

steps.

In this thesis work, standard ceramic methods were attempted to prepare

$Ca_2Mn_2O_5$, as we had not previously investigated this approach. The target reaction is:

$$3/2 \; CaO + \tfrac{1}{2} \; CaF_2 + \tfrac{1}{2} \; Mn_2O_3 + MnO_2 \rightarrow \mathbf{Ca_2Mn^{3+}Mn^{4+}O_5F}$$
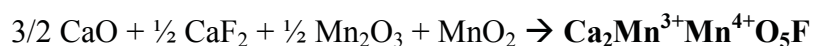
In this attempted synthesis the starting materials were combined according to their

stoichiometric mole equivalents and thoroughly mixed in a mixer mill. A sample of paste

weighing 1.8 g was pressed into a pellet, and placed in a Ni crucible on top of a sacrificial

mixed reactant powder. The crucible was placed into a Ni boat that was inserted into an

alumina tube, in turn placed into a Thermolyne 59300 tube furnace. The reaction was run

under argon gas using the following furnace program (R = Ramp function, L =

Temperature level, D = Dwell function):

Step 1	R1 – Step function	L1 – 70°C	D1 – 0 hrs.
Step 2	R2 – 60°C/hr.	L2 – 800°C	D2 – 48 hrs.
Step 3	R3 – 60°C /hr.	L3 – 1150°C	D3 – 72 hrs.
Step 4	R4 – 40°C /hr.	L4 – 200°C	D4 – 0 hrs
Step 5	R5 – Step function	L5 – 70°C	D5 – End

The product of this reaction was a mixture of grey powder, which was analyzed

using a Rigaku Miniflex X-ray powder diffractometer. The resulting diffraction pattern

is shown in **Figure 4.1**.
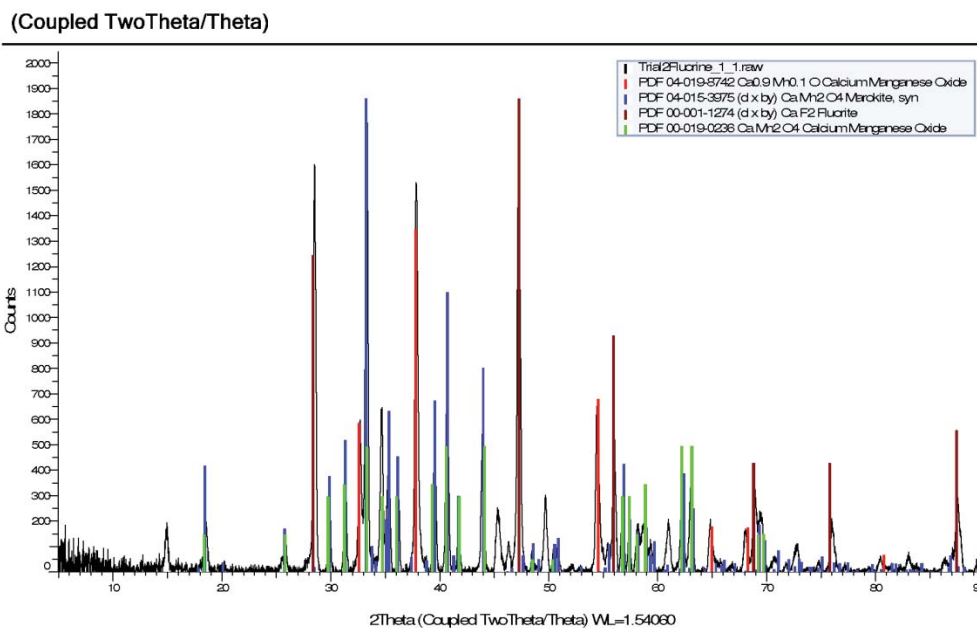
Fig 4.1 X-ray powder diffraction pattern from attempted preparation of $Ca_2Mn^{3+}Mn^{4+}O_5F$. Database matches are as follows:

- $Ca_{0.9}Mn_{0.1}O$ (red lines), PDF 04-019-8742, Cubic, Space group: $Fm\overline{3}m$ (225), Unit cell parameter: a = 4.755 Å.
- $CaMn_2O_4$ (blue lines), PDF 04-015-3975, Orthorhombic, Space group: Pbcm (57), Unit cell parameters: a = 3.149 Å, b = 9.980 Å, c = 9.660 Å.
- CaF_2 (brown lines), PDF 00-001-1274, Cubic, Space group: $Fm\overline{3}m$ (225), Unit cell parameter: a = 5.450 Å.
- $CaMn_2O_4$ (green lines), PDF 00-019-0236, Tetragonal, Space group: not given, Unit cell parameters: a = b = 5.760 Å, c = 9.200 Å.

Perhaps not surprisingly, the direct synthesis for the preparation of

$Ca_2Mn^{3+}Mn^{4+}O_5F$ through the route discussed above failed. This is because other

compounds, likely more thermodynamically stable, formed preferentially.

4.4 Attempted Synthesis of $Ca_2Mn^{3+}Mn^{4+}O_4N$

For the proposed preparation of an oxynitride mixed phase of $Mn^{+3, +4}$, standard

ceramic methods were again attempted, although in this case under reaction in ammonia:

$2CaCO_3 + \frac{1}{2}\ Mn_2O_3 + MnO_2 + NH_3 \rightarrow \mathbf{Ca_2Mn^{3+}Mn^{4+}O_4N} + 3/2\ H_2O + 2\ CO_2$.
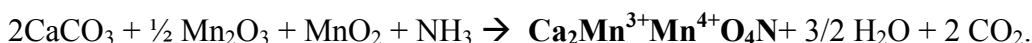
The reactants were weighed and combined in a stoichiometric ratio, and thoroughly mixed in a mixer mill to achieve a paste that was pressed into a pellet using a hydraulic pellet press. The pellet was then placed in a Ni crucible in turn placed in a high temperature programmable tube furnace (Mellen, NACCI series) programed according to the following conditions (R = Ramp function, L = Temperature level, D = Dwell function):

Step 1	R1 – Step function	L1 – 70°C	D1 – 0 hrs.
Step 2	R2 – 60°C/hr.	L2 – 800°C	D2 – 48 hrs.
Step 3	R3 – 60°C /hr.	L3 – 1150°C	D3 – 72 hrs.
Step 4	R4 – 40°C /hr.	L4 – 200°C	D4 – 0 hrs
Step 5	R5 – step function	L5 – 70°C	D5 – End

The final product consisted of green powder which was analyzed in the Rigaku Miniflex X-ray powder diffractometer. The resulting diffraction pattern is shown in **Figure 4.2.**

As no nitrogen-containing phases were observed in the product mixture according to the X-ray data in Figure 4.2, it appears that NH_3 did not react. Repeated attempts to prepare $Ca_2Mn^{3+}Mn^{4+}O_4N$ through the direct synthesis using this route were unsuccessful. As a result of this research, it was concluded that the synthesis of $CaMn_2O_4N$ and $Ca_2Mn_2O_5F$ through direct ceramic methods is not favorable, usually resulting in preferential formation of simpler compounds. Therefore other routes must be investigated, such as fluorine insertion reactions of $LaMnO_3$ as discussed in the next section.

(Coupled TwoTheta/Theta)
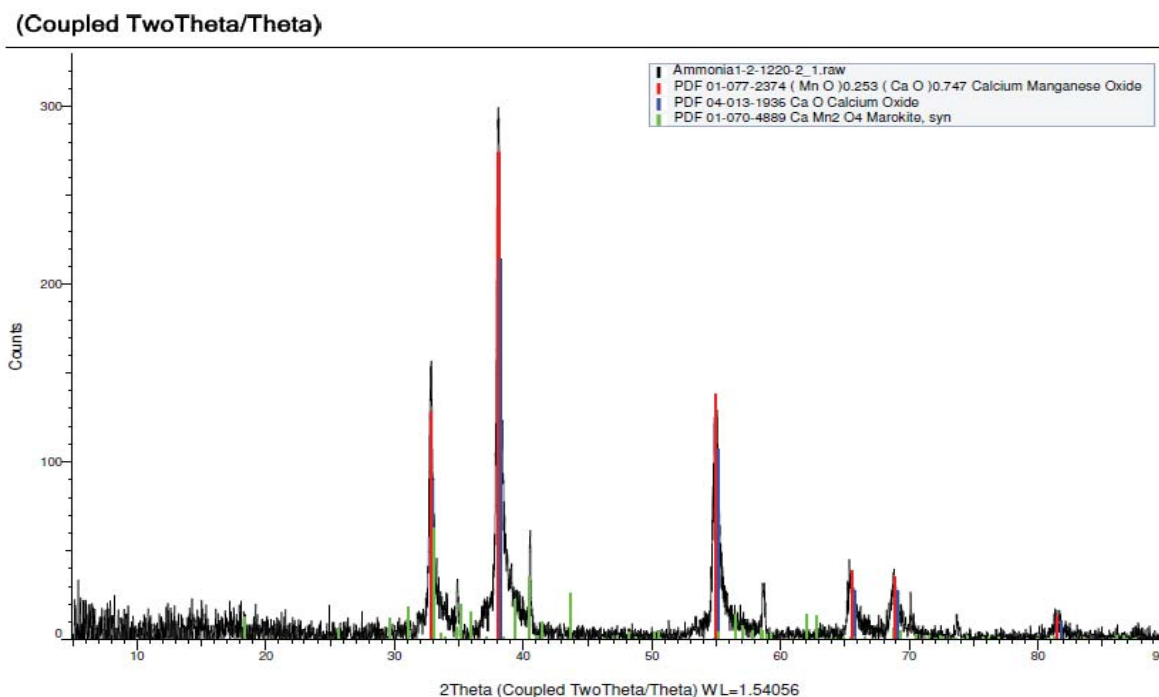
Fig. 4.2 X-ray powder diffraction pattern from attempted preparation of $Ca_2Mn^{3+}Mn^{4+}O_4N$. Database matches are as follows:

- $Ca_{0.747}Mn_{0.253}O$ (red lines), PDF 01-077-2374, Cubic, Space group: $Fm\overline{3}m$ (225), Unit cell parameter: a = 4.72 Å.
- CaO (blue lines), PDF 04-013-1936, Cubic, Space group: $Fm\overline{3}m$ (225), Unit cell parameter: a = 4.706 Å.
- $CaMn_2O_4$, PDF 01-070-4889, Orthorhombic, Space group: Pbcm (57), Unit cell parameters: a = 3.1546(6) Å, b = 9.988(2) Å, c = 9.6769(19) Å.

4.5 Synthesis of LaMn₂O₆F via Fluorine Insertion of LaMnO₃

From its tolerance factor of 0.989 (see Table 4.1), the composition $La_2Mn_2O_6F$

may be expected to be cubic with the structure predicted to have the oxide ions at normal

anion positions of a perovskite-related lattice, and the 'excess' fluoride ions at interstitial

positions. The positioning of fluoride ions into interstitial sites of an oxide can occur

through fluorine insertion reactions (Greaves and Francesconi, 1998). Thus in this thesis

work, a systematic study was conducted on low temperature fluorine insertion reactions

of $LaMnO_3$ using CuF_2, XeF_2, and PVDF (polyvinylidene difluoride) as fluorinating

agents. According to Tsujimoto et al. (2012), these compounds have been previously used as fluorinating agents in various perovskite-related systems. The $LaMnO_3$ starting material used for this thesis work was obtained from Sigma Aldrich (98% purity), and the powder X-ray diffraction pattern verifying phase purity for the as-received $LaMnO_3$ is shown in **Figure 4.3**. Results for the fluorine insertion reactions are discussed in the sub sections that follow.
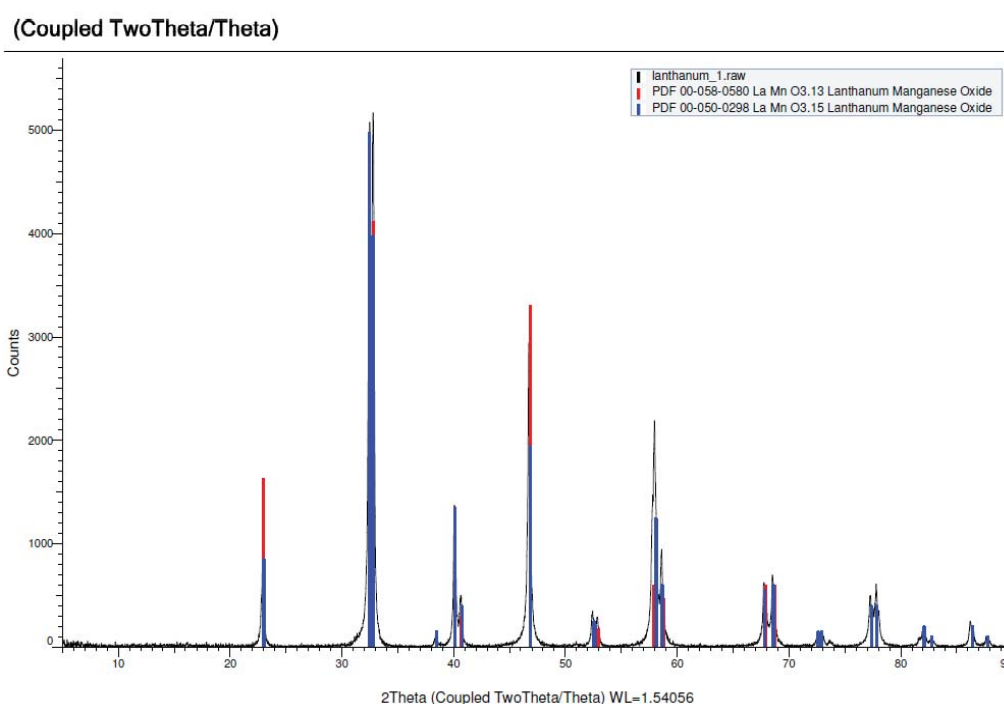
Fig. 4.3 X-ray powder diffraction pattern of as-received $LaMnO_3$. The database verified a pure phase with closely matched peaks of:

- $LaMnO_{3.13}$ (red lines), PDF 00-058-0580, Rhombohedral, Space group: $R\overline{3}c$ (167), Unit cell parameters: a = 5.5159 Å, c = 13.2868 Å.
- $LaMnO_{3.15}$ (blue lines), PDF 00-050-0298, Rhombohedral, Space group: $R\overline{3}c$ (167), Unit cell parameters: a = 5.5219 Å, c = 13.3327(58) Å.

4.6 Attempted Fluorine Insertion of $LaMnO_3$ Using CuF_2

Li and Greaves (2000) combined CuF_2 with $Sr_3Ru_2O_7$ in stoichiometric proportion to produce $Sr_3Ru_2O_7F_2$ via fluorine insertion. The $Sr_3Ru_2O_7$ precursor has a

layered perovskite-related structure (i.e., Ruddlesden-Popper phase) with an orthorhombic lattice. The product compound contained F atoms in interstitial positons, and retained the orthorhombic lattice but with expanded cell volume.

In this research we investigated the use of CuF_2 for fluorine insertion of $LaMnO_3$. The procedure starts with first mixing 0.0080 moles of $LaMnO_3$ with 0.0041 moles of CuF_2 for the following proposed reaction:

$$LaMnO_3 + \tfrac{1}{2}\, CuF_2 \rightarrow \mathbf{La_2Mn^{3+}Mn^{4+}O_6F} + \tfrac{1}{2}\, Cu.$$

The mixture was subjected to a maximum temperature of 400°C with a step-wise cooling through the following furnace program (R = Ramp function, L = Temperature level, D = Dwell function):

Step 1	R1 – Step function	L1 – 70°C	D1 – 0 hrs.
Step 2	R2 – 100°C /hr.	L2 – 400°C	D2 – 6 hrs.
Step 3	R3 – 15°C /hr.	L3 – 300°C	D3 – 6 hrs.
Step 4	R4 – Step function	L4 – 70°C	D4 – End

Upon completion of the reaction, the products yielded a mixture of a grey powder slurry which was analyzed via X-ray powder diffraction. The resulting X-ray diffraction powder pattern is shown in **Figure 4.4.**

Examination of the powder diffraction data shows that the reaction products consisted mainly of a cation deficient $LaMnO_3$ phase with composition $La_{0.946}Mn_{0.946}O_3$. This phase is isostructural with starting material, although slight oxidation of Mn^{3+} to Mn^{4+} appears to have occurred. Fluorine apparently is present only within the observed LaF_3 phase. Weaker lines were best indexed as a CuO phase. No Cu metal was detected. These results imply that Cu^{2+} displaced La^{3+} from one-third of the $LaMnO_3$ starting

material present, but there is no evidence of an Mn_2O_3 phase in the PXRD data that would likely be present if such a reaction occurred:

$$\text{1/3 LaMnO}_3 + \text{½ CuF}_2 \rightarrow \text{1/3 LaF}_3 + \text{½ CuO} + \text{1/6 Mn}_2\text{O}_3 \text{ (?)}$$
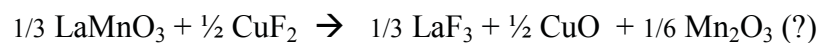
According to Brisdon *et al.* (1998), many reactions of fluorinating agents with manganese oxoanions produce MnO_3F, which is a liquid at room temperature so that its formation here would not have been detected in the X-ray diffractometer. In this case, the reaction which occurred would be:

$$\text{¼ LaMnO}_3 + \text{½ CuF}_2 \rightarrow \text{¼ LaF}_3 + \text{¼ MnO}_3\text{F}_{(liq)} + \text{½ Cu}.$$
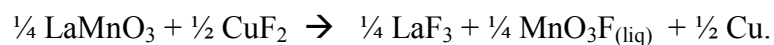
The reaction here appears to be unsupported due the lack of observation of Cu metal in the product mixture. However, further reaction could have occurred that oxidized the Cu to CuO, perhaps due to O_2 contamination during the reaction.

(Coupled TwoTheta/Theta)
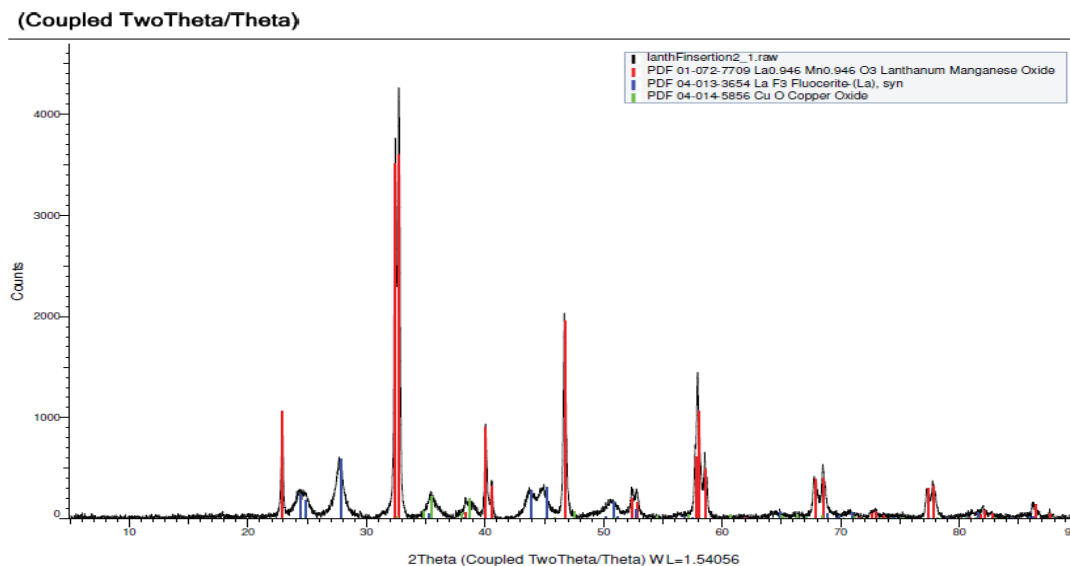
Fig. 4.4 X-ray powder diffraction pattern for attempted fluorine insertion of as-received $LaMnO_3$ using CuF_2. The product consists predominantly of an apparently cation deficient $LaMnO_3$ phase (red lines), with the presence of LaF_3 (blue lines) and CuO (green lines). The specific phases identified were:

- $La_{0.946}Mn_{0.946}O_3$, PDF 01-072-7709, Rhombohedral, Space group: $R\bar{3}c$ (167), Unit cell parameters: a = 5.5179(6) Å, c = 13.3463 (7) Å
- LaF_3, PDF, 04-013-3654, Hexagonal, Space group: $P\bar{3}c1$ (165), Unit cell parameters: a = 7.139 Å, c = 7.266 Å
- CuO, PDF 04-014-5856, Monoclinic, Space group: C2/c (15), Unit cell parameters: a = 4.794(3) Å, b = 3.362(1) Å, c = 5.228(2) Å, β = 99.79°.

4.7 Attempted Fluorine Insertion of LaMnO₃ Using XeF₂

Ardashnikova *et al*. (1995) prepared the superconducting oxyfluoride

$Sr_2CuO_2F_{2+\delta}$ through fluorination of Sr_2CuO_3 via solid state reactions with excess XeF_2 in

the low temperature range of 100-220°C. Further reaction to 400°C decomposed the

oxyfluoride mainly to $SrCuO_3$ and SrF_2. In this thesis work, we proposed to utilize XeF_2

for fluorine insertion of $LaMnO_3$ according to the reaction:

$$LaMnO_3 + \frac{1}{2}\ XeF_2 \rightarrow \mathbf{La_2Mn^{3+}Mn^{4+}O_6F} + \frac{1}{2}\ Xe$$

Room Temperature Reaction

Upon mixture (under Ar in the glove bag) of 0.008 moles of $LaMnO_3$ and 0.00413

moles of pure XeF_2 in a Ni crucible, reaction occurred immediately at room temperature.

It was discovered that the straight wall nickel crucible started becoming hot immediately

upon mixture of reactants. Therefore, instead of inserting the crucible into the tube

furnace for further heating, the product mixture was immediately prepared for analysis in

the Rigaku Miniflex Power Diffractometer, yielding the resulting pattern shown in
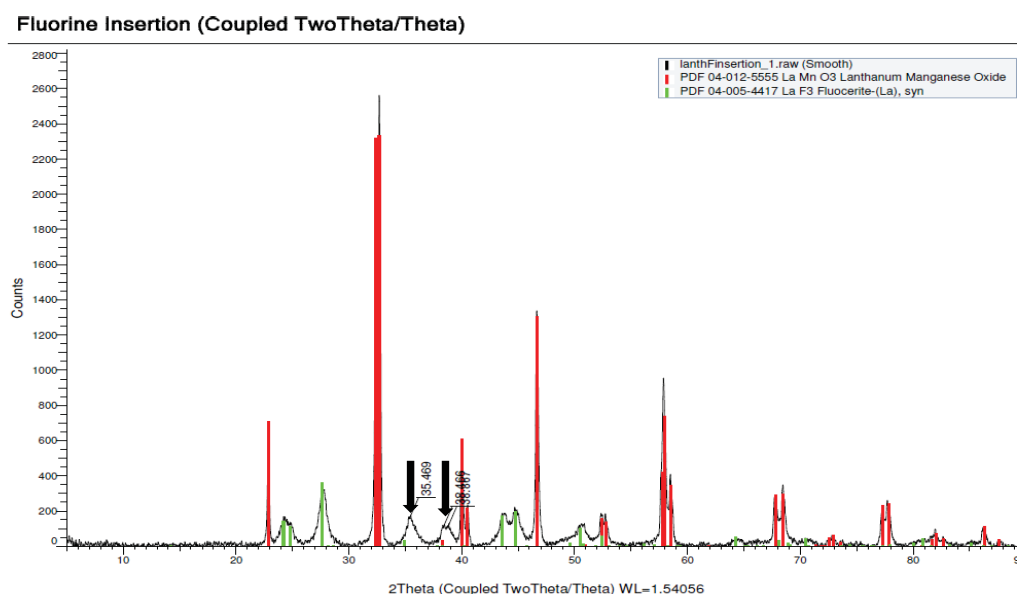
Figure 4.5.

Fig. 4.5 X-ray powder diffraction pattern for attempted fluorine insertion of as-received $LaMnO_3$ using XeF_2 at room temperature. The peaks at 2Theta = 35.469° and 38.887° (marked by arrows) appear to be identical to the peaks identified as CuO in Figure 4.4 above, and were matched accordingly (not shown) although no Cu should have been present. The main phases identified through database match were:

- $LaMnO_3$ (red lines), PDF 04-012-5555, Rhombohedral, Space group: $R\bar{3}c$ (167), Unit cell parameters: a = 5.5251(4) Å, c = 13.3531(6) Å.
- LaF_3 (green lines), PDF 04-005-4417, Hexagonal, Space group: $P\bar{3}c1$ (165), Unit cell parameters: a = 7.185(1) Å, c = 7.351(1) Å.

The PXRD pattern showed that the same peaks (with similar peak shape) identified as CuO in Figure 4.4 above were again present here. These peaks are positioned at 2Theta = 35.469º and 38.887º (marked by arrows on the pattern), with a nearby peak at 38.466º being due to $LaMnO_3$. Despite the fact that no Cu should have been present in this reaction using XeF_2 instead of CuF_2 as the fluorinating agent, thorough analysis showed that the best match was again CuO. Thus, CuO is evidently present as a contaminant in the PXRD sample that produced the pattern in Figure 4.5.

If it is again assumed that MnO_3F is a product of the reaction, now with XeF_2 as the fluorinating agent (Brisdon *et al*., 1998), and if the apparent CuO peaks are ignored, the reaction consistent with the PXRD pattern and original reactant mixture is:

¼ $LaMnO_3$ + ½ XeF_2 + 3/4 $LaMnO_3$ (unreacted) → ¼ LaF_3 + ¼ $MnO_3F_{(liq)}$ + ½ $Xe\uparrow$ + 3/4 $LaMnO_3$ (unreacted)
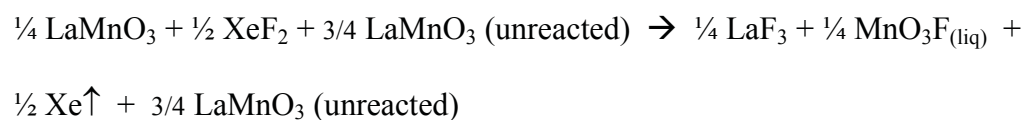
The oxidation of Mn^{3+} to Mn^{7+} via reduction of Xe^{2+} must be highly reactive, such that this accounts for the spontaneity of the reaction at room temperature.

Room Temperature Reaction Followed by Further Heating

In order to further investigate the reaction above, a fresh sample of as-received $LaMnO_3$ was reacted with XeF_2 at room temperature in a glove bag under Ar. The resulting product mixture (presumably the same as above) was then heated to a maximum temperature of 400°C according to the following furnace program (R = Ramp function, L = Temperature level, D = Dwell function):

Step 1	Step function	L1 – 70°C	D1 – 0 hrs.
Step 2	R2 – 100°C/hr.	L2 – 400°C	D2 – 6 hrs.
Step 3	R3 – 15°C/hr.	L3 – 300°C	D3 – 6 hrs.
Step 4	R4 – Step function	L4 – 70°C	D4 – End

The post-heated product mixture was analyzed using a Rigaku Miniflex II diffractometer, with the resulting pattern shown in **Figure 4.6**.
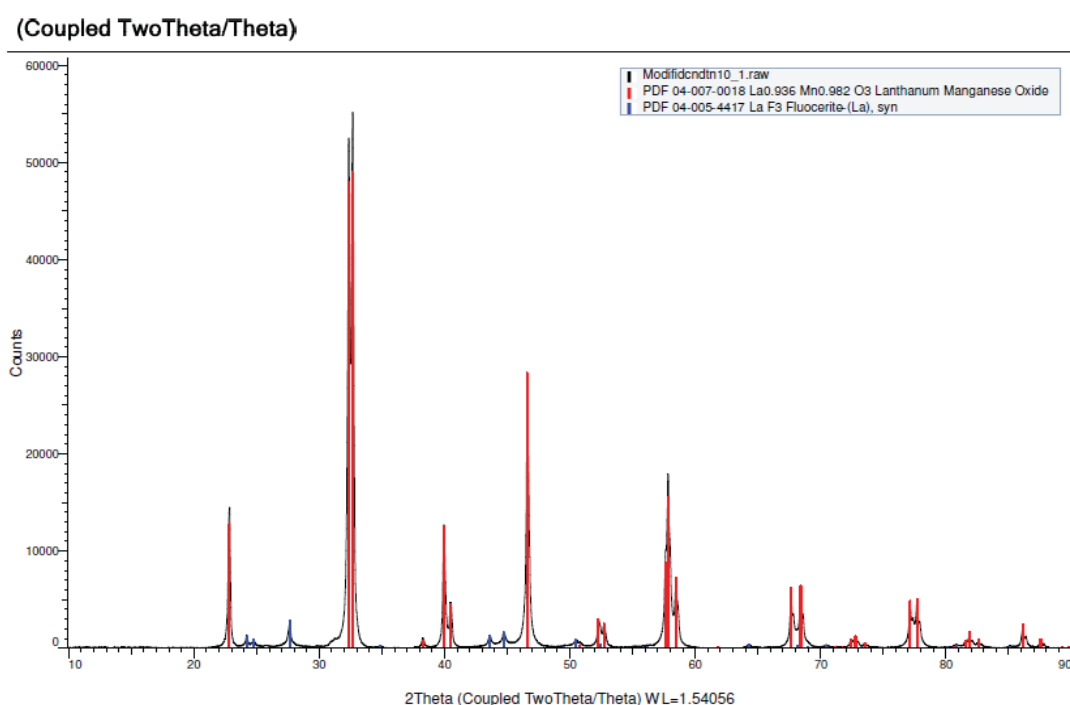
Fig. 4.6 X-ray powder diffraction pattern for attempted fluorine insertion of as-received $LaMnO_3$ using XeF_2 and heating to 400°C. $LaMnO_3$ and LaF_3 were again the main phases observed, as also seen in the diffraction pattern for the room temperature preparation shown in Figure 4.5. Note however that the unknown peaks at 2Theta = 35.469° and 38.466°/38.887° are now absent. The specific database matches are:

- $La_{0.936}Mn_{0.982}O_3$ (red lines), PDF 04-007-0018, Rhombohedral, Space group: $R\overline{3}c$ (167), Unit cell parameters: a = 5.5362 Å, c = 13.3598 Å.
- LaF_3, PDF 04-005-4417, Hexagonal, Space group: $P\overline{3}c1$ (165), Unit cell a = 7.185(1) Å, c =7.351(1) Å.

Immediately evident from the diffraction pattern is that the peaks assigned to CuO in the reactions above are now absent, while the only products identified are again a rhombohedral $LaMnO_3$ phase and LaF_3. Loss of peaks matched to CuO in the previous experiment (i.e. using XeF_2 at room temperature without further heating) would seem to suggest that perhaps the peaks are actually due to a phase that is volatile at the 400°C heating temperature. However, several attempts to match the peaks in question in Figures 4.4 and 4.5 to phases in the PDF database consistently reveal CuO as the best match. This suggests that CuO was a contaminant in at least the XeF_2 room temperature case, and was never present in the second trial just described.

Qualitative comparison of Figures 4.5 and 4.6 indicates that the peak intensities of LaF_3 in Figure 4.6 appear weaker relative to the $LaMnO_3$ peaks compared to the case in Figure 4.5. This turn suggests that during the heating process, *some* LaF_3 reacted, perhaps according to either of the following reactions:

$$3/4\ LaMnO_3 + ¼\ LaF_3 + ¼\ MnO_3F \rightarrow\ LaMnO_3 + ½\ F_2\uparrow$$

or

$$LaF_3 + MnO_3F \rightarrow LaMnO_3 + 2F_2\uparrow .$$
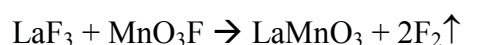
4.8 Fluorine Insertion of LaMnO₃ Using PVDF

Tsujimoto *et al*. (2012) in their review of oxyfluoride perovskite chemistry noted several studies in which PVDF (polyvinylidene difluoride) was successfully used as a fluorinating agent to produce manganite compounds such as $LaSrMnO_4F_2$. In order to synthesize $LaMn_2O_6F$, we therefore proposed the following reaction mechanism:

$$2LaMnO_3 + (PVDF) \rightarrow \mathbf{La_2Mn^{3+}Mn^{4+}O_5F}$$
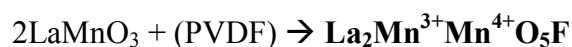
The reactants were weighed and mixed in a glove bag under argon gas. Specifically,

2.000g (0.008267 moles) of $LaMnO_3$ was combined with 0.397g (0.006202 moles) of

CH_2CF_2 (PVDF monomer). This represents a mole ratio of 1:1.333 of $LaMnO_3$ to

CH_2CF_2, such that PVDF was present in excess. The reaction was run under dynamic

flow of Ar according to the following furnace program (R = Ramp function, L =

Temperature level, D = Dwell function):

Step 1	Step function	L1 – 70°C	D1 – 0 hrs.
Step 2	R2 – 100°C /hr.	L2 – 400°C	D2 – 6 hrs.
Step 3	R3 – 15°C /hr.	L3 – 300°C	D3 – 6 hrs.
Step 4	R4 – Step function	L4 – 70°C	D4 – End

The final product consisted of black powder, which was analyzed via X-ray powder

diffraction using a Rigaku Miniflex II diffractometer. The resulting diffraction pattern is

shown in **Figure 4.7**.

Three features of the PXRD pattern shown in Figure 4.7 are significant. The first

is that most of the as-received rhombohedral-type $LaMnO_3$ phase used a starting reagent

transformed completely to a cubic perovskite-type phase in the course of the reaction.

The remainder reacted with PVDF to give LaF_3 and presumably MnO_3F, according to the

weak LaF_3 peaks present. The second significant feature is that the cubic $LaMnO_3$ peaks

are shifted to the left relative to the database positions, indicating that the unit cell of our

phase is somewhat larger than the literature phase. Third, the weak, unmatched peaks

marked by the arrows in the PXRD pattern are consistent with doubling of the cubic

lattice, as further discussed below.
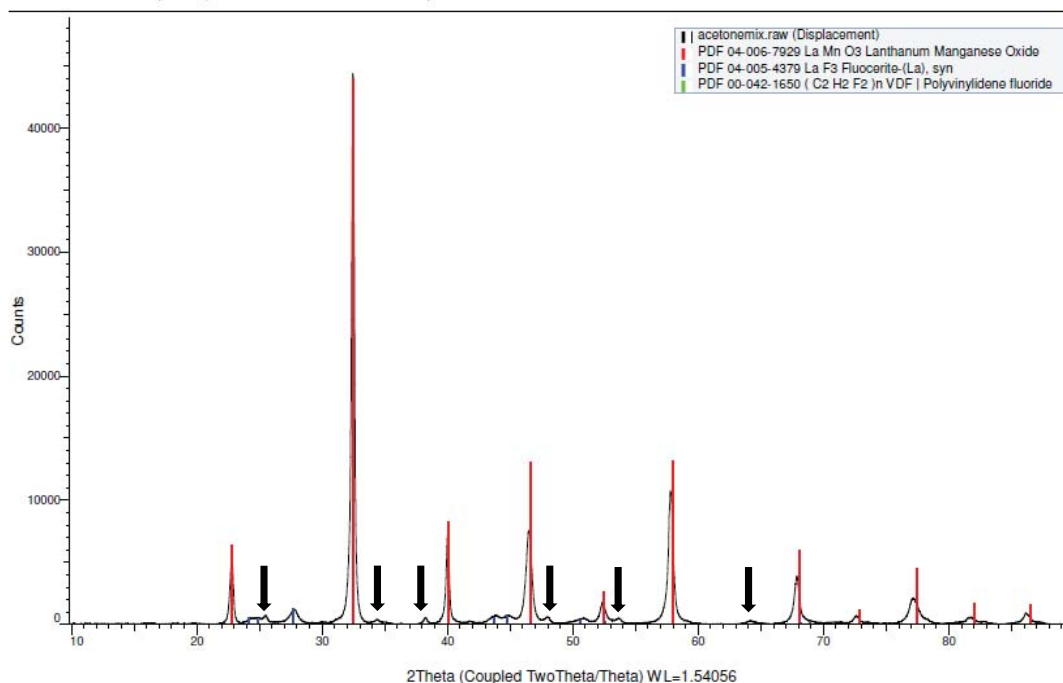
Fig 4.7 X-ray powder diffraction pattern for attempted fluorine insertion of as-received LaMnO$_3$ using PVDF (polyvinylidene difluoride). No PVDF remained in the product mixture. Black arrows mark weak, non-matched peaks which are consistent with a doubled unit cell relative to cubic LaMnO$_3$ (a = 3.894 Å). Database matches are as follows:

- LaMnO$_3$ (red lines), PDF 04-006-7929, Cubic, Space group: Pm$\overline{3}$m (221), Unit cell parameter: a = 3.894 Å.
- LaF$_3$ (blue line), PDF 04-005-4379, Hexagonal, Space group: P6$_3$cm (185), Unit cell a = 7.16(1) Å, c = 7.36(1) Å.

The fact that as-received rhombohedral LaMnO$_3$ transformed completely to a

cubic perovskite-type phase is consistent with the hypothesis discussed above in Section

4.2 that La$_2$Mn^{3+}Mn^{4+}O$_6$F should be cubic. This is because oxidation of some Mn^{3+} to

smaller Mn^{4+} increases the tolerance factor of 0.961 expected for LaMnO$_3$ to 0.989 for

La$_2$Mn^{3+}Mn^{4+}O$_6$F, with the latter value being consistent with a cubic lattice.

Furthermore, some expansion of the lattice would be expected with F atoms introduced

into interstitial sites, and this is consistent with the fact that the experimental peaks have shifted left relative to the closest database match for cubic $LaMnO_3$.

Of course, the composition $La_2Mn^{3+}Mn^{4+}O_6F$ implies doubling of the ideal cubic-type perovskite lattice, whereas the predominant phase in Figure 4.8 is of the ideal cubic-type. However, close examination of the data in Figure 4.7 shows very weak peaks (marked by arrows) that appear to be consistent with doubling of the ideal cubic lattice. **Table 4.2** compares the positions (as 2Θ values) of these weak experimental peaks in Figure 4.7 to the positions calculated for a cubic lattice with a = 7.788 Å, i.e. doubled relative to a = 3.894 Å for cubic-perovskite-type $LaMnO_3$. It is seen that the peak positions match fairly well, with the experimental peaks all shifted to the left relative to the calculated peaks, consistent with the positions of the experimental vs. database peaks for the bulk phase. Note also that the (hkl) values given for the calculated peaks could not be indexed according to corresponding (h/2 k/2 l/2) values needed for the cubic subcell, as they each contain at least one odd number.

These results suggest that most of the product of this reaction is cubic $LaMnO_3F_x$, where 'x' is a fraction such that the lattice expanded only slightly. A calculation of tolerance factor shows that the minimum value of x needed for $LaMn^{3+}_{(1-x)}Mn^{4+}_xO_3F_x$ such that the tolerance factor is at least 0.985 (i.e., minimum typical value consistent with a cubic phase) is x = 0.43. As for the weak peaks discussed above, these can be accounted for by local doubling of the lattice based upon appropriate random distribution of interstitial F atoms.

Table 4.2 Analysis of weak PXRD peaks marked by arrows in Figure 4.7

Experimental Peak Position ($2\Theta_{exp}$, degrees)	Calculated Peak Position for Doubled Cubic Cell, a = 7.788 Å ($2\Theta_{exp}$, degrees) / (hkl)	Difference ($2\Theta_{exp} - 2\Theta_{calc}$)
25.397	25.555 / (210)	-0.158
34.377	34.522 / (300)	-0.145
38.255	38.299 / (311)	-0.044
47.918	48.133 / (322)	-0.215
53.599	53.904 / (412)	-0.305
64.199	64.365 / (432)	-0.166

4.9 Conclusions and Future Work

For three of the four fluorination reactions discussed above, in which either CuF_2 or XeF_2 were used as fluorinating agents, the main products were isostructural rhombohedral $LaMnO_3$ phases varying only slightly in composition. The second most common phase formed was LaF_3, which was the predominant fluoride-containing phase in these reactions. Oxidation of Mn^{3+} in these reactions was likely to Mn^{7+} in MnO_3F, which is formed as a liquid under conditions of these reactions. This in turn implies that the fluorinating agents in these cases were too reactive, taking the oxidation of Mn^{3+} past the Mn^{4+} target. Based on these factors, along with the close match in PDF database vs. experimental peaks for the $LaMnO_3$ phases, it can be concluded that no fluorinated $LaMnO_3F_x$-related compositions were formed in any of these three reactions.

The most promising result in this study involved the use of PVDF (polyvinylidene difluoride) as the fluorinating agent. In this reaction, the as-received rhombohedral $LaMnO_3$ lattice completely transformed to a cubic phase with a slightly expanded unit cell relative to the PDF database phase, as expected for F-insertion of $LaMnO_3$. In addition, weak peaks on the PXRD pattern were consistent with a doubled cubic $LaMnO_3$-type lattice, as might be expected from the $La_2Mn_2O_6F$ target composition.

Future work should focus on the use of PVDF to fluorinate $LaMnO_3$ starting material, and should emphasize direct experimental verification that a fluorinated phase was successfully prepared. For example, magnetic susceptibility measurements could be taken to detect the presence of Mn^{4+} in the lattice. Another approach would be to utilize TEM (Transmission Electron Microscopy) techniques. The TEM, as compared to SEM (Scanning Electron Microscopy), would enable the use of selected area electron diffraction to first verify that the sample under study is a $LaMnO_3$ phase vs. other phases that may be present in the bulk sample, such as LaF_3. The electron diffraction patterns, coupled with high resolution images, would also reveal any local distortions due to the presence of interstitial F atoms in the lattice. Finally, EDS (Energy Dispersive Spectroscopy) analysis could be utilized to qualitatively detect the presence of F in the sample lattice.

CHAPTER FIVE

CRYSTAL CHEMISTRY OF STRONTIUM AND STRONTIOUM-MIXED

METAL NITRIDE FLUORIDE COMPOUNDS

5.1 Introduction

This research concentrated on preparation and structural characterization of strontium nitride fluorides, including for the first time Group II bimetallic phases. Specific bimetallic phases studied were SrMgNF and SrCaNF, although SrMgNF was not successfully prepared. The first compound to be prepared was single crystalline rocksalt-type Sr_2NF, discussed in the next section, and doubled cubic SrCaNF was also prepared.

5.2 Single Crystalline Rocksalt-type Sr_2NF

Preparation

The first preparation in this series of experiments was to reproduce previous results by Wagner (2002). In this study, single crystals of Sr_2NF were prepared using the following reaction:

$$3Sr + SrF_2 + N_2 \rightarrow 2Sr_2NF.$$

Wagner (2002) reported a structure with an ordered rocksalt-type lattice, with N and F atoms ordered along the cell-axes such that the unit cell parameter was approximately doubled relative to the disordered rocksalt Sr_2NF phase reported by Ehrlich *et al*. (1971). This 'doubled-cubic lattice' was a new result for the Group II metal N-F system, and was later reported as a Ca_2NF phase in report by Jack *et al*. (2005), and more recently by Al-Azzawi *et al*. (2017).

For the current preparation, the mass of strontium used was 2.00 g, corresponding to 0.0228 moles of strontium. This was used to calculate the amount SrF_2 to be used (3:1 Sr/SrF_2 mole ratio) which turned out to be 0.955 g. The reactants were weighed and put into a straight wall nickel crucible in the presence of argon gas, and sealed in a glove bag. The crucible was then placed in a silica reaction tube, which was in turn placed into the Thermolyne tube furnace and reacted according to the following program (R = Ramp Rate, L = Temperature Level, and D = Dwell Time):

Step 1:	R1 – Step Function	L1 – 70°C	D1 – 0 hours
Step 2:	R2 – 80°C /hr.	L2 – 1000°C	D2 – 1 Hour
Step 3:	R3 – 80°C /hr.	L3 – 200°C	D3 – 1 Hour
Step 4:	R4 – 60°C /hr.	L4 – 1000°C	D4 – 4 Hours
Step 5:	R5 – 15°C /hr.	L5 – 200°C	D5 – 0 Hours
Step 6:	R6 – Step Function	L6 –70°C	D6 – End

Dynamic flow of argon gas was running from Step 1, but switched to nitrogen gas at Step 4, so before starting the reaction the time that would elapse during each step was calculated in order to determine the time to switch the gases.

The products of this reaction consisted of a mixture of yellow crystals and black/gray powder, which was identified as strontium nitride. Among the many yellow crystals, a single crystal was selected and immediately placed on a slide in the glove bag under argon, and put on a glass slide with a drop of mineral oil. It was further analyzed using the Bruker D8 QUEST single-crystal diffractometer equipped with a 100 cm^2 Photon 100 CMOS detector, and a high brightness Mo IµS Incoatec microsource with a 2.4-kW sealed tube X-ray source using MoKα radiation (0.71073 Å), operated at 50 kV and 1 mA. An Oxford Cryostream 700plus system was used to keep the crystal in a

flowing nitrogen stream at 100K throughout the experiment to prevent chemical

decomposition. Data collection and cell refinement were performed using APEX2

(version 2013.4-1), and SADABS (embedded within APEX2) was used to scale the data

and apply absorption correction. Data were collected to a resolution of 0.51Å.

Single Crystal X-ray Data Collection and Structure Refinement

Structure solution and refinement was straightforward and yielded a disordered

rocksalt-type structure with space group Fm$\overline{3}$m (No. 225) and unit cell parameter of a =

5.3051(2) Å. The unit cell parameter is very close to the value of a = 5.38 Å reported by

Ehrlich et al. (1971) for their powder sample, presumably collected at room temperature.

X-ray data for our sample was collected at 100 K, which likely accounts for some

shrinkage of the unit cell.

The final R1 (F) value was 0.0123 for all 51 data (4 parameters), and

wR2 (F^2) = 0.0240. A structure plot is shown in **Figure 5.1**. To our knowledge, this is

the first structure analysis of single crystalline rocksalt-type Sr$_2$NF.
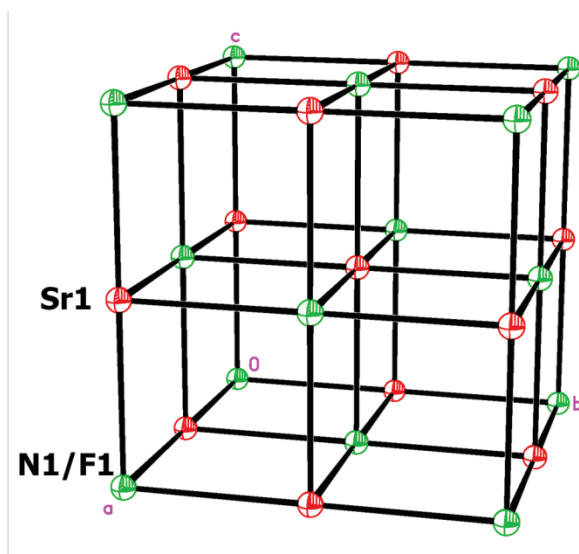
Fig. 5.1 Unit cell plot for Sr$_2$NF, disordered rocksalt-type structure with a = 5.3051(2) Å. Nitrogen and fluorine atoms share a position; 50% ellipsoids.

5.3 Single Crystal Preparation and Structural Analysis of Bimetallic SrCaNF

Preparation

The mixed-metal nitride-fluoride compound, SrCaNF, was prepared for the first time through the reaction below:

$$SrF_2 + 2Ca + Sr + N_2 \rightarrow 2SrCaNF$$
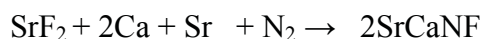
Strontium and calcium are both Group II elements and have melting points of 777°C and 842°C, respectively. The reaction was run at 1000°C, as was the case for previous preparations of Sr_2NF by Wagner (2002) and Ca_2NF by Nicklow *et al.* (2001) and Jack *et al.* (2005). The starting materials were mixed in a glove bag under Ar, as the Ca and Sr metal starting materials are very air sensitive. The reagents were first weighed in the order of SrF_2, 1.43 g (0.0114 moles); Ca, 0.91 g (0.0228 moles) and Sr,1.0 gram (0.0114 moles), and then placed in a 5 mL, straight-walled Ni crucible. The crucible was then placed in a Ni boat and inserted into the reaction tube, which was in turn inserted into the Thermolyne tube furnace. The reaction proceeded using the following furnace program (R = Ramp Rate, L = Temperature Level, and D = Dwell Time):

Step 1:	R1 – Step Function	L1 – 70°C	D1 – 0 Hours
Step 2:	R2 – 60°C /hr.	L2 – 1000°C	D2 – 8.0 Hours
Step 3:	R3 – 40°C /hr.	L3 – 200°C	D3 – 0 Hours
Step 4:	R4 – 60C /hr.	L4 – 1000°C	D4 – 4 Hours
Step 5:	R5 – 15°C /hr.	L5 – 200°C	D5 – 0 Hours
Step 6:	R6 – Step Function	L6 – 25°C	D6 – End

The final product consisted of a mixture of red, yellow, and grey crystals and the smaller amount of unreacted starting material. The colourless crystals appeared to be SrF_2 the grey crystals appeared to be a mixture of chunks of unreacted material and so their

composition was not determined. A yellow crystal was thoroughly analyzed via single crystal X-ray diffraction, and found to refine as a SrCaNF phase, as discussed below.

X-ray Data Collection

X-ray data were collected on a Bruker D8 QUEST single-crystal diffractometer equipped with a 100 cm^2 Photon 100 CMOS detector, and a high brightness Mo IμS Incoatec microsource with a 2.4-kW sealed tube X-ray source using MoKα radiation (0.71073 Å) operated at 50 kV and 1 mA. An Oxford Cryostream 700plus system was used to keep the crystal in a flowing nitrogen stream at 100K throughout the experiment to prevent chemical decomposition. Data collection and cell refinement were performed using APEX2 (version 2013.4-1), and SADABS (embedded within APEX2) was used to scale the data and apply absorption correction. Data were collected to high resolution of 0.48 Å.

Refinement and Structure Analysis

The structure was solved via direct methods using the SHELXTL-2014 suite of programs. The crystal was metrically cubic (a = 10.3404(10) Å), and was refined in space group Fd$\bar{3}$m (No. 227). Additional crystallographic and refinement data are provided in **Table 5.1**, with further structural refinement details discussed below. Atomic coordinates, refined occupancy factors, and anisotropic and equivalent isotropic displacement parameters are listed in **Table 5.2**.

The first evidence of a bimetallic composition was the unit cell parameter, which lies at approximately the midpoint between the doubled cubic phases of Ca$_2$NF (a = 10.0215(8) Å) reported by Jack *et al*. (2005) and the brownish-yellow phase of Sr$_2$NF (a

= 10.692(5) Å) reported by Wagner (2002). The space group found for the SrCaNF crystal also indicated that it likely had the doubled cubic cell as observed for the Sr_2NF and Ca_2NF single metallic 'end members'. The unit cell plot for SrCaNF is shown in **Figure 5.2**, from which certain structural features are evident. First, it is seen that doubling of the rocksalt-type cell is due to ordering of N and F atoms along [100], while Sr and Ca atoms essentially share a position. Actually, R values dropped slightly when Sr and Ca positions were allowed to refine independently to sites only 0.14 Å apart, with displacement parameters constrained to be equal. An interstitial fluorine atom (the F2 position on Figure 5.1) is present in the structure, as previously discussed for doubled cubic Ca_2NF and Sr_2NF phases in Chapter 2. Unlike the previous cases, however, in which interstitial F atoms were located at tetrahedral sites equidistant from the metal atoms, here the interstitial F atoms are disordered between four positions surrounding the tetrahedral site. Finally, disorder is also present at F1 (octahedral) sites, which are displaced to F1A positions when a nearby interstitial site is occupied. Disorder in the fluorine positions in the lattice will be further discussed below.

Table 5.1. Crystal data and structure refinement for SrCaNF

Identification code	17OKSrCaNFb_0m
Empirical formula	CaSrNF
Formula weight	160.71
Temperature	100(2) K
Wavelength	0.71073 Å
Crystal system	Cubic
Space group	$Fd\bar{3}m$
Unit cell dimensions	a = 10.3404(3) Å
Volume	1105.64(10) Å^3
Z	16
Density (calculated)	3.862 Mg/m^3
Absorption coefficient	21.072 mm^{-1}
F(000)	1184
Crystal size	0.0663 × 0.0553 × 0.0190 mm^3
Theta range for data collection	3.413 to 47.755°.
Index ranges	-21<=h<=21, -20<=k<=21, -21<=l<=20
Reflections collected	18879
Independent reflections	291 [R(int) = 0.0613]
Completeness to theta = 25.242°	100.0 %
Absorption correction	Multi-scan
Refinement method	Full-matrix least-squares on F^2
Data / restraints / parameters	291 / 3 / 23
Goodness-of-fit on F^2	1.161
Final R indices [I>2sigma(I)]	R1(F)[a] = 0.0171, wR2(F^2)[b] = 0.0406
R indices (all data)	R1(F)[a] = 0.0207, wR2(F^2)[b] = 0.0440
Extinction coefficient	0.00022(7)
Largest diff. peak and hole	0.568 and -1.062 eÅ^{-3}

[a]$R_1(F) = \Sigma ||F_o| - |F_c|| / \Sigma |F_o|$ with $F_o > 4.0\sigma(F)$. [b]$wR_2(F^2) = [\Sigma[w(F_o^2 - F_c^2)^2]/\Sigma[w(F_o^2)^2]]^{1/2}$ with $F_o > 4.0\sigma(F)$, and $w^{-1} = \sigma^2(F_o)^2 + (W \cdot P)^2 + T \cdot P$, where $P = (Max(F_o^2, 0) + 2F_c^2)/3$, W = 0.0141, and T = 7.55.

Table 5.2. Atomic coordinates (x 10^4), occupational[a], and anisotropic[b] and equivalent isotropic[c] displacement parameters (Å^2x 10^3) for SrCaNF.

Atom	Fd$\bar{3}$m (No. 227) Wyckoff Site	Refined Occ. Factor	No. Atoms/ Unit Cell	x	y	z	U^{11}	U^{23}	U(eq)
Sr1	32e	0.514	16.45	4943(1)	7557(1)	-57(1)	6(1)	0(1)	6(1)
Ca1	32e	0.486	15.55	4865(4)	7635(4)	-135(4)	6(1)	-1(1)	6(1)
F1	16c	0.579	9.26	5000	5000	0	26(4)	0(3)	19(1)
F1A	32e	0.175	5.60	5265(9)	5265(9)	265(9)			26(4)
F2	32e	0.092	2.94	5930(30)	5930(30)	930(30)	19(1)	6(2)	90(30)
N1	16d	0.943	15.09	5000	0	0	90(30)	50(30)	6(1)
F3	16d	0.057	0.91	5000	0	0	6(1)	0(1)	6(1)

[a]Occupancy factors were refined for all atoms. Occupancies for N and F were constrained for charge balance. [b]The anisotropic displacement parameter (ADP) is expressed as $\exp[-2\pi^2(h^2a^{*2}U_{11} + k^2b^{*2}U_{22} + l^2c^{*2}U_{33} + 2hka^*b^*U_{12} + 2hla^*c^*U_{13} + 2klb^*c^*U_{23})]$; $U_{11} = U_{22} = U_{33}$ and $U_{23} = U_{13} = U_{12}$, except $U_{23} = -U_{12}$ for Sr1/Ca1 atoms. All ADPs were freely refined without use of restraints. Atoms Sr1 and Ca1, and N1 and F3, which share a site, were constrained to have identical ADPs. [c]U_{eq} is defined as one third of the trace of the U_{ij} orthogonalized tensor.

Occupancy factors are listed in Table 5.2, and were refined for all positions. As expected from the unit cell parameters, the occupancy factors for the Sr and Ca atoms are close to equal. From the table, the overall unit cell composition is:

$Sr_{16.45}Ca_{15.55}N_{15.09}F_{18.72}$, or $Sr_{1.03}Ca_{0.97}N_{0.94}F_{1.17}$ relative to the empirical ideal formula of SrCaNF. It is evident from the refined composition that excess fluorine is present in the lattice and there is a deficiency of nitrogen relative to the ideal formula. Thus a non-stoichiometry defect is in place, similar to the case for Ca_2NF in recent work by Al-Azzawi (2016). Looking more closely at occupancies by site shows that 1.14 (= 16-

14.86) fluorine vacancies are present at the F1/F1A disordered octahedral site per unit

cell: $Sr_{16.45}Ca_{15.55}$ $(N_{15.09}F_{0.91})$ oct site $(F_{14.86})$ disordered oct site $(F_{2.94})$ int. site. Thus it appears that
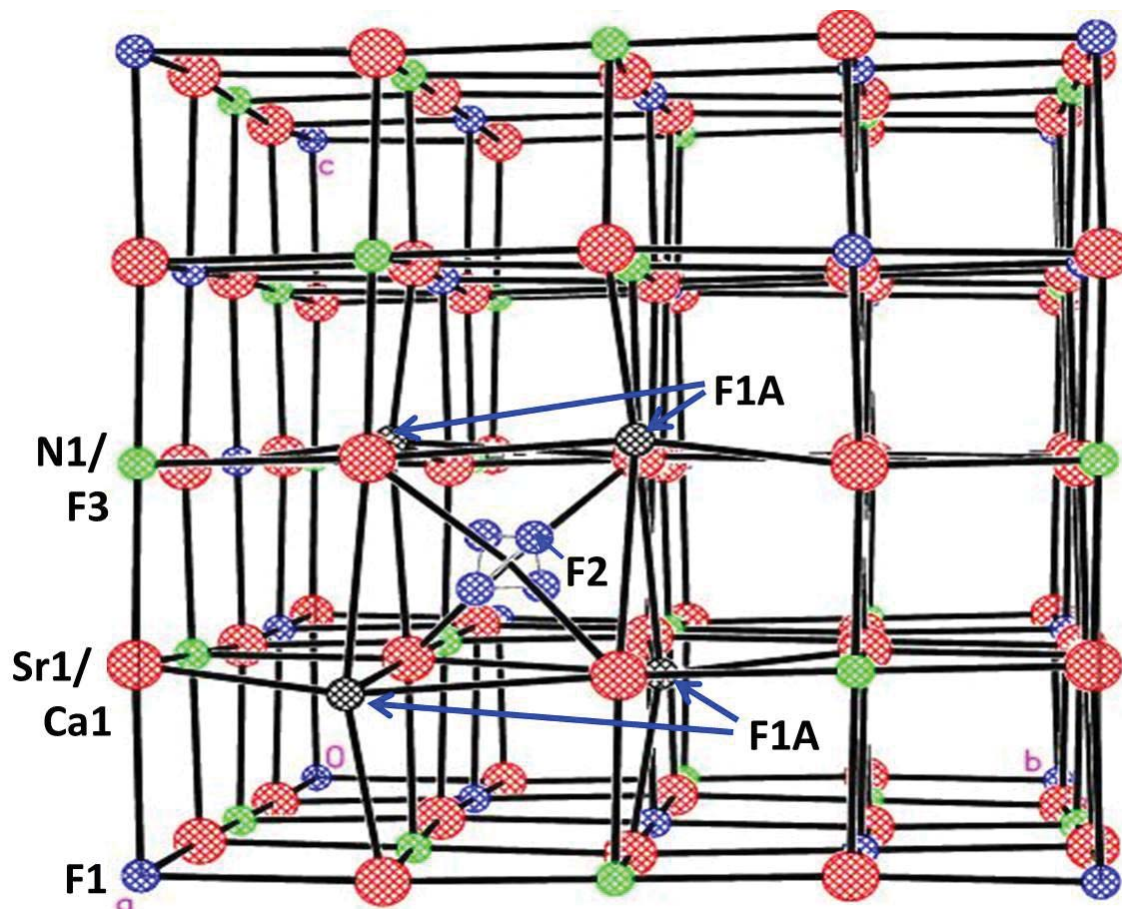
Fig. 5.2 Unit cell plot of SrCaNF, showing that each F2 interstitial atom is disordered among four F2 crystallographically equivalent positions oriented around a vacant, tetrahedral lattice position at x, y, z = 0.875, 0.375, 0.375. The position is marked by the point at which four bonds from nearby Sr atoms meet. F1A atoms displaced from the F1 site due to the presence of a nearby F2 atom are also shown. Sr and Ca (not shown) atoms are actually on slightly separate positions, only 0.14 Å apart.

1.14 of the 2.94 interstitial fluorine atoms present per unit cell for this crystal are from

nearby F1 sites due to a Frenkel defect, which in general refers to an equal number of

anion (or cation) vacancies and interstitials in a lattice. This is the first nitride-fluoride

observed with both types of defect present in the same crystal.

Figure 5.3 shows the local coordination environment around Sr/Ca, and the

disorder at the Sr/Ca, F1/F1A, and F2 sites is evident in the figure. In particular, F1/F1A

and F2 are highly disordered. Although displacement of F1 atoms to nearby positions

was observed in the previous study on Ca_2NF by Al-Azzawi (2016), the disorder at the

F2 interstitial site has not been observed in any previous study on doubled cubic M_2NF

(M = Ca, Sr) compounds. As this is also the first bimetallic ordered rocksalt phase

reported, the disorder at F2 may be related to the disorder at the Sr/Ca positions. Also,

the fact that each of four possible F2 positions in Figure 5.2 lies close to one of the F1

positions suggests that F2 may be positioned at whichever site is closest to a vacancy.

An attempt to refine the F2 at the ideal tetrahedral site (see above) led to large spherical

anisotropic displacement encompassing the four disordered sites, and a significantly

larger R value. Nevertheless, as the refinement showed only 1.14 vacancies per 2.94

interstitial F2 atoms per unit cell, it is possible that the F2 atoms are disordered around

the four positions shown when there is a nearby vacancy, and that they are positioned at

the ideal tetrahedral site otherwise. **Figure 5.4** shows the local environment for F2 atoms,

where it is seen that F2 is in a distorted tetrahedral coordination, with three short bonds of

2.218(5) Å to Sr or 2.358 Å to Ca(not shown), and one longer bond to each of these at

2.91(5) Å and 2.732(4) Å, respectively.
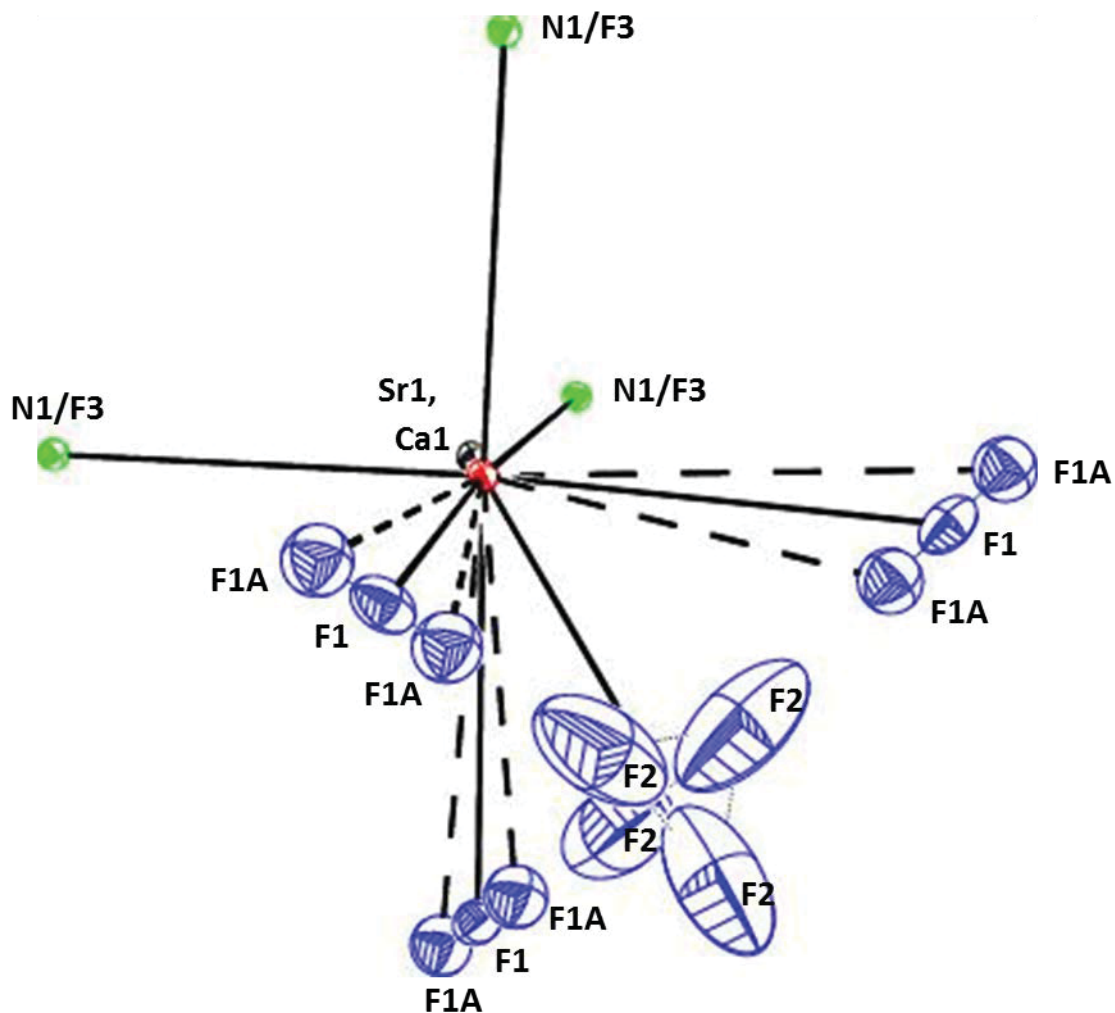
Fig 5.3 Local coordination environment for Sr/Ca in SrCaNF: Displacement of F1 to F1A positions 0.475 Å on either side of F1 is shown; disorder of F2 atoms among four crystallographically distinct positions is evident; 25% ellipsoids.
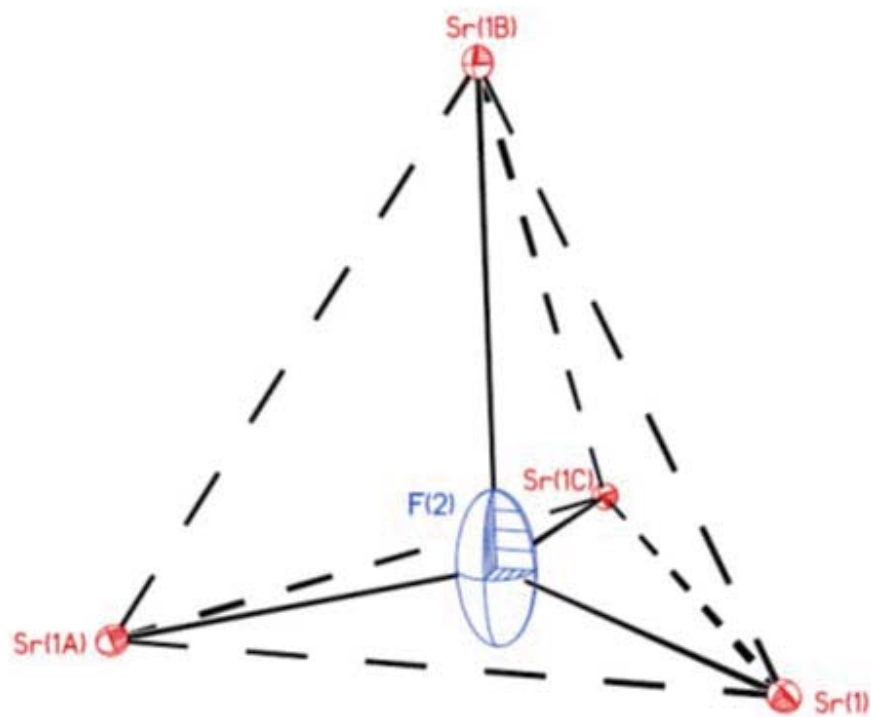
Fig 5.4 Local coordination environment for F2 (Ca atoms not shown) in SrCaNF: The F2 atom is displaced from the ideal tetrahedral position; there are 3 short Sr/Ca-F bonds at 2.2 Å, and one long bond at 2.9 Å; 25% ellipsoids.

5.4 Attempted Synthesis of SrMgNF

After the success of getting single crystals from the previous system, other

attempts were made to use bimetallic SrMNF, with M = other Group II cations. The first

attempt was to model the reaction used in the Sr-Ca system but to substitute magnesium

for calcium and so the reaction was as follows:

$$MgF_2 + 2Sr + Mg + N_2 \rightarrow 2SrMgNF$$
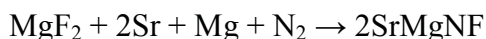
With the melting points of magnesium fluoride being 1263 ºC, Sr at 777 ºC and Mg at

650 ºC, the reaction was run at 1000 ºC in order to ensure that reactants formed a melt for

single crystal growth. The reactants were weighed and mixed in the nickel crucible in an

inert atmosphere of argon gas while confined to a glove bag. The nickel crucible was then

placed in the reaction tube and the following furnace program was used for the reaction

attempt (R = Ramp function, L = Temperature level, D = Dwell function):

Step 1	R1 – Step Function	L1 – 70°C	D1 – 0 hours
Step 2	R2 – 80°C/hr.	L2 – 1000°C	D2 – 1 Hour
Step 3	R3 – 80°C/hr.	L3 – 200°C	D3 – 1 Hour
Step 4	R4 – 60°C/hr.	L4 – 1000°C	D4 – 4 Hours
Step 5	R5 – 15°C/hr.	L5 – 200°C	D5 – 0 Hours
Step 6	R6 – Step Function	L6 – 70°C	D6 – End

For this reaction, 0.20 g of Mg, 2.0 g of Sr, and 0.71 g of MgF_2 was used, and the

final product consisted of black/grey powder mixed with some additional small grey

crystals, there was also a chunk of black mixture and what appeared to be some unreacted

starting material.

Attempted X-ray analysis of the small grey crystals failed. They were too small,

and multiple analyses trials showed they did not diffract well enough to obtain a unit cell

parameter. In fact, there did not appear to be any suitable single crystals for X-ray

diffraction in the product mixture. Various attempts to obtain single crystal data on a number of different crystals of appropriate size failed, it was concluded that these crystals were amorphous as they didn't diffract.

5.5 Summary and Future Work

While disordered rocksalt-type Sr_2NF has been well-known for some time from powder studies (see Chapter 2 discussion), this work represents the first quantitative single crystal study completed to our knowledge.

The results presented above for SrCaNF also represent the first bimetallic Group II nitride-fluoride phase to be successfully prepared with crystals of sufficient quality for thorough crystal chemical characterization via single crystal X-ray diffraction. The structure is highly disordered, consisting of combined non-stoichiometry and Frenkel defects not previously observed in this system. The disorder of the F atoms at the interstitial sites is also a new observation in Group II N-F crystal chemistry. It is important that future work includes compositional analysis via EDS analysis in order to verify a pure N-F anion composition (with no oxygen contamination), as well as to verify any excess fluorine present. .

Finally, future work must also include band structure calculations of both M_2NF and MM'NF mixed cation N-F phases to better characterize optical and electronic properties of these materials.

REFERENCES

Al-Azzawi, M. (2016). MS Thesis: <u>Synthesis and Characterization of Single Crystalline Metal Nitride Fluorides</u>, Youngstown State University.

Al-Azzawi M., Zeller M., Li, D., Wagner T. (2017). Crystal chemistry of ordered rocksalt-type Ca_2NF. *J. of Solid State Chem*., 254, 126-131.

Al-Mamouri, M., Edwards, P.P., Greaves, C., Slaski, M. (1994). Synthesis and superconducting properties of the strontium copper oxy-fluoride $Sr_2CuO_2F_{2+\delta}$. *Nature*. 369, 382–384.

Andersson, S. (1970). Magnesium nitride fluorides. *Journal of Solid State Chemistry*, 1(3-4), 306-309. DOI: 10.1016/0022-4596(70)90109-x.

Ardashnikova, E.I., Lubarsky, S.V., Denisenko, D.I., Shpanchenko, R.V., Antipov, E.V., van Tendeloo, G. (1995). A new way of synthesis and characterization of superconducting oxyfluoride $Sr_2Cu (O, F)_{4+\delta}$. *Physics*. C253, 259–265.

Bailey, A. S., Hughes, R. W., Hubberstey, P., Ritter, C., Smith, R. I., & Gregory, D. H. (2011). New ternary and quaternary barium nitride halides; synthesis and crystal chemistry. *Inorg. Chem*., **50**(19), 9545-9553. DOI: 10.1021/ic201264u.

Baker, (2006). Double exchange mechanism between Mn(+3) and Mn(+4) ions, through oxo bridge. <u>en.wikipedia</u> (accessed November 2017).

Baldini, M., Struzhkin, V.V., Goncharov, A.F., Postorino, P., Mao, W.L. (2011). Persistence of Jahn-Teller distortion up to the insulator to metal transition in $LaMnO_3$. *Physics Rev Letter*., 106(6):066402.

Bragg's Law <u>http://skuld.bmsc.washington.edu/merritt/bc530/bragg</u>

Brogan, M. A., Hughes, R. W., Smith, R. I., & Gregory, D. H. (2012). Structural studies of magnesium nitride fluorides by powder neutron diffraction. *Journal of Solid State Chemistry*, 185, 213-218. doi:10.1016/j.jssc.2011.11.008.

Clark J, (2012). Structure of Graphite. Giant Covalent Structures [image] retrieved from <u>http://www.chemguide.co.uk/atoms/structures/giantcov.html</u>

CK-12 Foundation Retrieved July 24, 2017 <u>https://www.ck12.org/book/ck-12-physical-science-for-middle-school/section/9.1/</u>

Ehrlich, P., Linz, W., Seifert, H. (1971). Nitrofluoride der Schweren Erdalkalimetalle. *Naturwisenschanften*,58,219 Press, Avon.

Fäth, M., Freisem, S., Menovsky, A.A., Tomioka, Y., Aarts, J., Mydosh, J.A., (1999). Spatially inhomogeneous metal-insulator transition in doped manganites. *Science*, 285(5433):1540–1542.

Fang, C.M., Ramanujachary, K.V., Hintzen, H.T. (2003). *Journal of Alloys and Compounds*, Science Direct.

Fourteen Bravais lattices (https://www.seas.upenn.edu/~chem101/sschem/bravais.gif.

Galy, J. Jaccou, M. and Andersson, S. (1971). Nitrofluoride, Ca_2NF.oxynitrofluorinated solid solutions $Ca_2O_{2x}N_{1-x}F_{1-x}$,*C.R. Acad. Sc. Paris*, 272, 1657

Giant Covalent Structures. Retrieved November 14, 2017 from the www.chemguide.co.uk/atoms/structures/giantcov.

Goodenough, J., Longo, J.M. (1970). Magnetic and Other Properties of Oxides and Related Compounds. Landolt-Borstein Tabellen, New Series, Group 3, eds. Hellewege K-H, Hellewege AM (Springer, Berlin), Vol 4.

Greaves, C., Francesconi, M.G. (1998), Fluorine Insertion in Inorganic Materials, *Current Opinion in Solid State and Materials Science*, 3(2), 132-136.

Hwang, H.Y., Cheong, S.W., Ong, N. P., Batlogg, B. (1996). Spin-polarized intergrain tunneling in La-2/Sr-3(1)/3MnO3, *Phys. Rev. Lett.*, 77(10), 2041-2044.

Jack, D.R., Zeller, M., Wagner, T.R. (2005). Doubled-Cubic Ca_2NF. *Acta Cryst. C*, 61, I6-I8.

Jim Clark 2000 (modified October 2012) *Structure of Graphite*. Retrieved on November 14, 2017 from (www.chemguide.co.uk/atoms/structures/giantcov).

Lai, K., Nakamura, M., Kundhikanjana. W., Kawasaki, M., Tokura, Y., Kelly, M.A., Shen, Z.X. (2010). Mesoscopic Percolating Resistance Network in a Strained Manganite Thin Film. *Science*, 329(5988), 190–193.

Laue equation: http://electrons.wikidot.com/x-ray-diffraction.

Lee, M.M., Teuscher, J., Miyasaka, T., Murakami T.N., Snaith, H.J. (2012). Efficient Hybrid Solar Cells Based on Meso-Superstructured Organometallic Halide Perovskites. *Science*, 338(6107), 643-647.

Li, R.K., Greaves, C. (2000). Double-layer ruthenate $Sr_3Ru_2O_7F_2$ formed by fluorine insertion into $Sr_3Ru_2O_7$, *Physical Review B*, 62(6) 3811-3815.

Liu, X., Hong, R., Tian, C. (2008). Tolerance factor and the stability discussion of ABO_3-type ilmenite. *Journal of Materials Science*: *Materials in Electronics*, 20, 323.

Liu, Y.K., Yin, Y.W., Li, X.G. (2013). Colossal magnetoresistance in manganites and related prototype devices. *Chinese Physics B*, 22(8), 087502: 1-19.

Liu, Y.K., Yin, Y.W., Li, X.G. (2013). Colossal magnetoresistance in manganites and related prototype devices. *Chinese Physics B*, 22(8), 087502: 1-19.

Materials Science Tetrahedron Image, Wikimedia Commons. Retrieved July 24, 2017, fromhttps://commons.wikimedia.org/wiki/File:Materials_science_tetrahedron;structure,_processing,_performance,_and_proprerties.JPG.

Meneghini, C., Di Matteo, S., Monesi, C., Neisius, T., Paolasini, L., Mobilio, S., Natoli, C.R., Metcalf, P.A., Honig, J.M., (2005). Structural dicroism in the antiferromagnetic insulating phase of V_2O_3. *Physical Review*, B72, 033111.

Moreira, R.L., Dias, A. (2007) Comment on "Prediction of lattice constant in cubic perovskites". *J. of Physics and Chem. of Solids*, 68, 1617-1622.

Nicklow, R.A., T.R. Wagner, Raymond, C.C. (2001). Preparation and Single-Crystal Structure Analysis of Ca_2NF. *Journal of Solid State Chemistry*: 160, 134-38.

Osterloh, F.E., Parkinson, B.A. (2011). Recent developments in solar water-splitting photocatalysis. *MRS Bulletin*, 36(1), 17-22.

Pavarini, E., Koch, E., Anders, F., Jarrell, M.(Eds), (2012). Correlated Electrons: From Models to Materials, Vol. 2, Jülich Forschungszentrum, ISBN 978-3-89336-796-2.

Perovskites and Perovskite Solar Cells. Retrieved November 14, 2017, from www.ossila.com/pages/perovskites-and-perovskite-solar-cells-an-introduction.

Poeppelmeier, K.R., Leonowicz, M.E., Scanlon, J.C., Longo, J.M. (1982). Structure determination of $CaMnO_3$ and $CaMnO_{2.5}$ by X-ray and neutron methods. *Journal of Solid State Chem.,* 45(1), 71-79.

Ramirez, A.P. (1997). Colossal Magnetoresistance. *Journal of Physics: Condensed Matter*, 9(39), 8171-8199.

Seibel, H., and Wagner, T.R. (2004). Preparation and Crystal Structure of Ba_2NF. *Journal of Solid State Chemistry*, 177, 2772-776.

Shannon, R.D. (1976). Revised Effective Ionic Radii and Systematic Studies of Interatomic Distances in Halides and Chalcogenides. *Acta Cryst.*, A32, 751-767.

Strozewski, M. S. (2007). MS Thesis: Synthesis and crystal chemistry of $Ca_2NxO_{2-2x}F_x$ (x = 0 to 1) and other compounds. Youngstown State University.

Slater, P.R. (2002). Poly (vinylidene fluoride) as a reagent for the synthesis of K_2NiF_4-related inorganic oxide fluorides. *J. Fluor. Chem.*, *117*, 43–45.

Slater, P.R, Gover, R.K.B. (2002). Synthesis and structure of the new oxide fluoride $Sr_2TiO_3F_2$ from the low temperature fluorination of Sr_2TiO_4: An example of a staged fluorine substitution/insertion reaction. *J. of Materials Chem.*, 12(2), 291–294.

The Bragg's Law and Laue equation. Retrieved on November 14, 2017, from http://electrons.wikidot.com/x-ray-diffraction.

Tsujimoto Y., Yamaura K., Takayama-Muromachi T. (2012). Oxyfluoride Chemistry of Layered Perovskite Compounds. *Appl. Sci.* (2), 206-219.

Wagner, T. (2002). Preparation and single-crystal structure analysis of Sr_2NF. *Journal of Solid State Chemistry*, 169, 13-18.

Wolf, A. (2011). MS Thesis: <u>Investigations of a Novel Manganite Oxyfluoride and Other Ceramic Materials</u>, Youngstown State University.

Zener, C. (1951). Interaction between the d-Shells in the Transition Metals. II. Ferromagnetic Compounds of Manganese with Perovskite Structure. *Phys. Rev.*82, 403.